Article

Cell

Mechanisms of Anion Conduction by Coupled Glutamate Transporters

Graphical Abstract

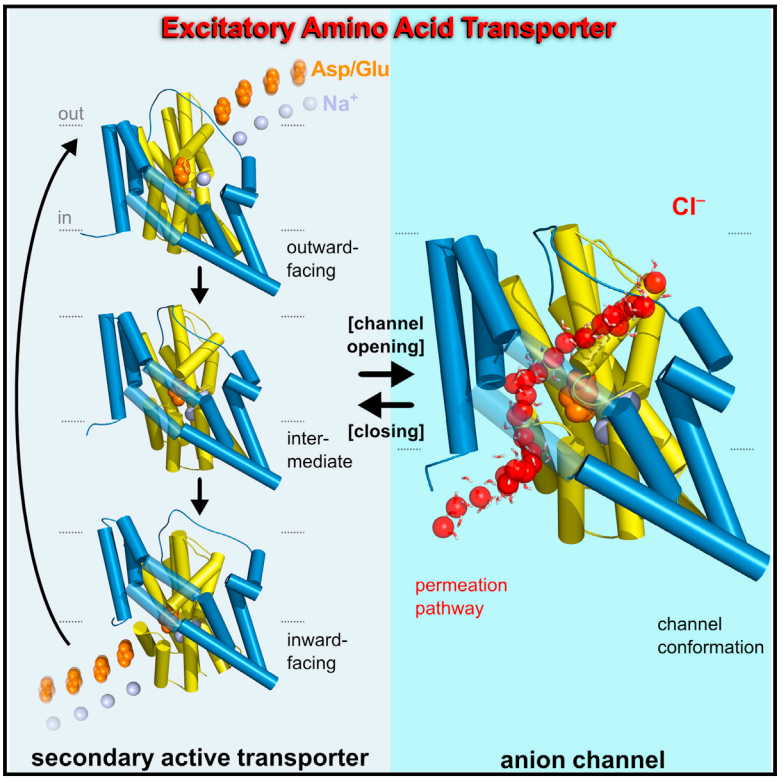

Authors

Jan-Philipp Machtens, Daniel Kortzak, ..., Rodolfo Briones, Christoph Fahlke

Correspondence

jan-philipp.machtens@gmx.de (J.-P.M.), c.fahlke@fz-juelich.de (Ch.F.)

In Brief

Excitatory amino acid transporters operate both as transporters and as anion-selective ion channels at synapses. A combination of simulations and experiments with prokaryotic and mammalian glutamate transporter homologs defines the anion conduction pathway and elucidates how a class of secondary active transporters can function as perfectly selective, gated anion channels.

Highlights

- Molecular dynamics simulations define anion-conducting transporter conformations
- Anion permeation occurs along a well-defined, conserved permeation pathway
- Transport intermediates open the channel via steric and hydrophobic gating
- Anion selectivity is achieved via a single, structurally conserved arginine

Machtens et al., 2015, Cell *160*, 542–553
January 29, 2015
http://dx.doi.org/10.1016/j.cell.2014.12.035

CellPress

Cell

Article

Mechanisms of Anion Conduction by Coupled Glutamate Transporters

Jan-Philipp Machtens,[1,2,3,*] Daniel Kortzak,[1] Christine Lansche,[1] Ariane Leinenweber,[2] Petra Kilian,[2] Birgit Begemann,[2] Ulrich Zachariae,[4] David Ewers,[2] Bert L. de Groot,[3] Rodolfo Briones,[3] and Christoph Fahlke[1,*]

[1]Institute of Complex Systems, Zelluläre Biophysik (ICS-4), Forschungszentrum Jülich, 52428 Jülich, Germany

[2]Institut für Neurophysiologie, Medizinische Hochschule Hannover, 30625 Hannover, Germany

[3]Computational Biomolecular Dynamics Group, Max Planck Institute for Biophysical Chemistry, 37077 Göttingen, Germany

[4]School of Engineering, Physics, and Mathematics and Division of Computational Biology, College of Life Sciences, University of Dundee, Dundee DD1 5EH, UK

*Correspondence: jan-philipp.machtens@gmx.de (J.-P.M.), c.fahlke@fz-juelich.de (Ch.F.)

http://dx.doi.org/10.1016/j.cell.2014.12.035

SUMMARY

Excitatory amino acid transporters (EAATs) are essential for terminating glutamatergic synaptic transmission. They are not only coupled glutamate/Na^+/H^+/K^+ transporters but also function as anion-selective channels. EAAT anion channels regulate neuronal excitability, and gain-of-function mutations in these proteins result in ataxia and epilepsy. We have combined molecular dynamics simulations with fluorescence spectroscopy of the prokaryotic homolog Glt_{Ph} and patch-clamp recordings of mammalian EAATs to determine how these transporters conduct anions. Whereas outward- and inward-facing Glt_{Ph} conformations are nonconductive, lateral movement of the glutamate transport domain from intermediate transporter conformations results in formation of an anion-selective conduction pathway. Fluorescence quenching of inserted tryptophan residues indicated the entry of anions into this pathway, and mutations of homologous pore-forming residues had analogous effects on Glt_{Ph} simulations and EAAT2/EAAT4 measurements of single-channel currents and anion/cation selectivities. These findings provide a mechanistic framework of how neurotransmitter transporters can operate as anion-selective and ligand-gated ion channels.

INTRODUCTION

Secondary active glutamate transport by excitatory amino acid transporters (EAATs) (Kanner and Sharon, 1978) terminates glutamatergic synaptic transmission and regulates glutamate concentrations within the CNS. EAATs can also function as anion-selective channels (Fairman et al., 1995; Wadiche and Kavanaugh, 1998), with EAAT anion channels regulating cell excitability and synaptic transmission (Picaud et al., 1995). Their physiological relevance is emphasized by the recent discovery that altered EAAT anion conduction is associated with episodic ataxia and epilepsy (Winter et al., 2012).

EAAT anion permeation occurs through a defined anion-selective conduction pathway (Kovermann et al., 2010), which is opened and closed through conformational changes coupled to transitions within the glutamate uptake cycle (Bergles et al., 2002; Machtens et al., 2011a; Otis and Kavanaugh, 2000). The channels are perfectly anion selective (Wadiche and Kavanaugh, 1998) and exhibit unitary current amplitudes, which are small but of a similar size range to those of specialized anion channels (Schneider et al., 2014). The five mammalian EAATs differ in their relative glutamate transport rates and anion currents, resulting in isoform-specific differentiation into efficient transporters associated with small macroscopic anion currents and low-capacity transporters that predominantly conduct anions (Mim et al., 2005). However, the functional properties of the underlying anion channels are very similar for each type (Schneider et al., 2014; Torres-Salazar and Fahlke, 2007), indicating conservation of the anion-conducting pore among functionally specialized transporters. So far, the localization of this conduction pathway, the underlying conformation of the transporter, and the mechanisms of anion permeation have not been identified.

We used molecular dynamics (MD) simulations to identify which conformations of the archeal glutamate transporter homolog Glt_{Ph} (Yernool et al., 2004) permit anion permeation and to characterize the molecular features of anion conduction. We analyzed the conformational changes leading to the formation of an anion-selective pore and observed ion permeation along this path in simulations. Using mutagenesis, fluorescence spectroscopy experiments on Glt_{Ph} and patch-clamp recordings on mammalian EAATs, we confirmed that the anion channel conformation we identified exists under experimental conditions and that this permeation pathway is utilized by both prokaryotic and mammalian glutamate transporters.

RESULTS

Molecular Dynamics Simulations Identify Anion-Conducting Conformations of Glt_{Ph}

Glt_{Ph} shares about 37% sequence identity with mammalian EAATs and is an accepted model of this class of transporters for studying secondary active transport and anion conduction (Boudker et al., 2007; Groeneveld and Slotboom, 2010; Ryan and Mindell, 2007; Yernool et al., 2004). High-resolution crystal

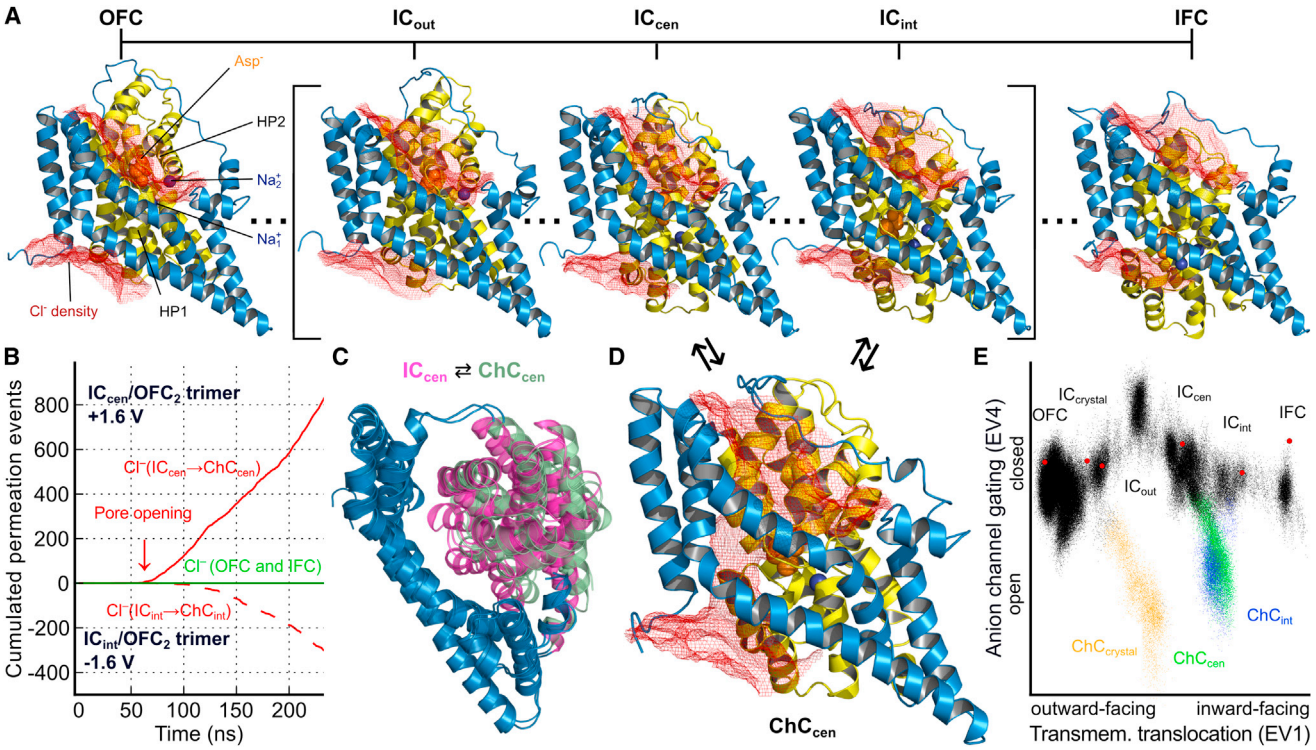

Figure 1. An Anion-Selective Conduction Pathway Is Formed by a Substrate Transport Intermediate

(A) Red isodensity meshes illustrate the Cl^- distribution (0.2σ) in MD simulations at +1.6 V around substrate-bound Glt_{Ph} monomers in various conformations (trimerization domain shown in blue; transport domain shown in yellow). The other two monomers, water molecules, lipids, and ions were omitted for clarity. Nonconductive outward-facing (OFC), inward-facing (IFC), and intermediate conformations (ICs; derived using essential dynamics sampling of the transition from OFC to IFC) are shown in side view.

(B and C) Ion permeation (B) and conformational change (C) of IC_{cen} during transition to an open channel conformation (overlay of IC_{cen} and ChC_{cen}, top view) upon application of a membrane potential (±1.6 V).

(D) Transitions of ICs into open channel conformations (ChCs) containing an anion-selective pathway occur at positive and negative potentials.

(E) Visualization of all trajectories (the OFC–IFC translocation/essential dynamics sampling simulation and separate MD simulations of OFC, IC_{out}, $IC_{crystal}$, IC_{cen}, IC_{int}, IFC, and of the ChCs of the intermediates) in the principal component space by projection onto the first (EV1) and fourth (EV4) eigenvectors, corresponding to translocation and pore formation, respectively. Black dots represent nonconducting conformations. Blue, green, and orange dots denote frames in MD trajectories, where Cl^- permeation through the respective ChC conformation was observed. Note that the point density is biased by the number and length of simulations initiated from the various starting conformations (red circles) and therefore does not provide information on energetics.

See also Figures S1, S2, and S3 and Movie S1.

structures revealed a trimeric assembly, with each subunit containing eight transmembrane helices (TM) and two hairpin loops (HP) (Yernool et al., 2004). Analysis of different conformations demonstrated that substrate translocation involves a large-scale (~18 Å) rotational translational movement of the substrate-harboring transport domain relative to the static trimerization domain (Crisman et al., 2009; Reyes et al., 2009).

We used all-atom MD simulations capable of directly simulating ion flux driven by transmembrane voltages (Kutzner et al., 2011) to investigate anion permeation in substrate-bound Glt_{Ph}. Simulations were performed using various Glt_{Ph} conformations in the presence of 1 M NaCl on either side of the membrane. Positive and negative membrane potentials (initially ±1.6 V; later ±800 mV) applied to increase anion permeation rates had no detrimental effects on the stability of the system (Figure S1 available online), in good agreement with the results of other simulation studies (Jensen et al., 2012). Within a total simulation time of >8 μs, no Cl^- permeation events were observed for the known outward- (OFC) and inward-facing (IFC) conformations at membrane potentials up to ±1.6 V, indicating that none of these states is anion conducting (Figures 1A and 1B; Extended Experimental Procedures). We concluded that translocation intermediates might correspond to the precursors of anion-conducting conformational states and simulated the OFC–IFC transition to obtain novel intermediate conformations (ICs) using essential dynamics sampling (Amadei et al., 1996). In these simulations, the transporter was driven along the first eigenvector (EV1)—representing transmembrane translocation of the transport domain—from a principal component analysis (PCA) of the conformational changes of transporter monomers in simulations on OFC and IFC (Figures 1A, S1C, and S1D). Because individual subunits function independently within the trimeric assembly (Erkens et al., 2013; Grewer et al., 2005), translocation simulations were performed on a single monomer—with the other two remaining in the OFC. These simulations correctly sampled the recently crystallized Glt_{Ph} intermediate ($IC_{crystal}$, minimum

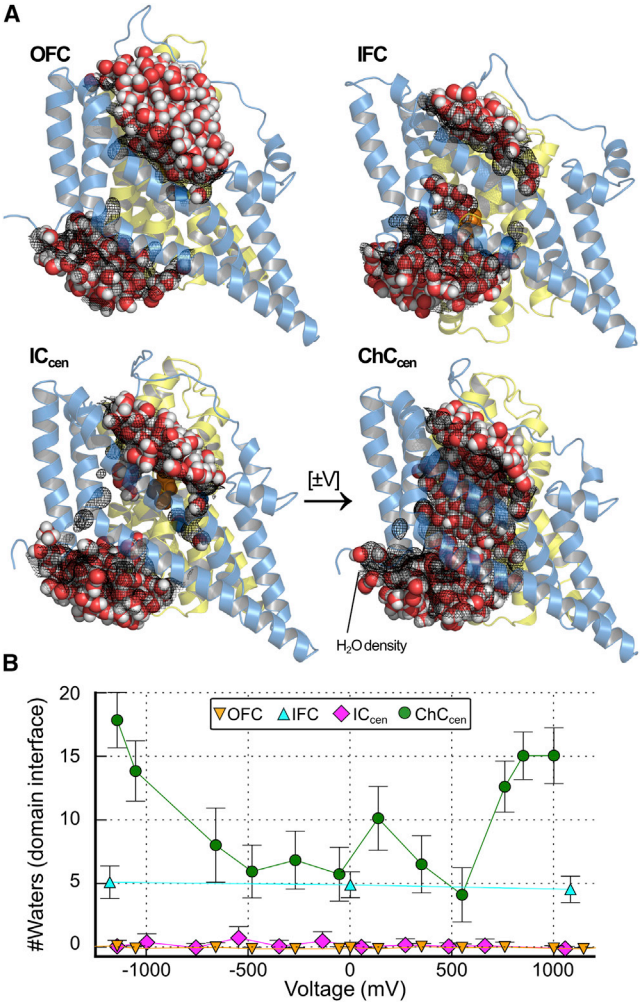

Figure 2. Hydrophobic Gating of the Anion Permeation Pathway

(A) Representative (spheres) and averaged (black mesh) water distribution in the transport/trimerization domain interface of Glt_{Ph} in various conformations (side view).

(B) Voltage-dependent occupancy of the interface core region by water molecules (counted within a cylindrical slab; each data point corresponds to a 100 ns simulation). Note that increased water numbers in ChC, but not in IFC, result in the formation of a continuous water bridge between the extra- and intracellular space (A). Error bars indicate the SD of the water molecule counts during the simulations.

monomeric root-mean-square deviation [RMSD] of 1.3 Å). This demonstrates the existence and stability of translocation intermediates (Verdon and Boudker, 2012) and validates the simulated transition pathway (Figure S2C). We then chose three intermediates, IC_{out} (similar to $IC_{crystal}$), IC_{cen}, and IC_{int}, from our trajectory that were equally distributed between the OFC and IFC, and, together with $IC_{crystal}$, subjected them to further MD under transmembrane voltage (Figures 1A and S1).

All intermediates were impermeable to Cl^- and remained closed for hundreds of nanoseconds in the absence of membrane voltage (Figures 1A and S1G; Extended Experimental Procedures). However, for $IC_{crystal}$, IC_{cen}, and IC_{int}, lateral movement of the transport domain occurred 70–300 ns after applying membrane potentials $\geq \pm 1.3$ V. These conformational changes resulted in open channel conformations (designated here as $ChC_{crystal}$, ChC_{cen}, or ChC_{int}) that were centrally localized on the translocation reaction coordinate and that exhibited an anion-selective conduction pathway at the interface between the trimerization and transport domains, near the tip of HP1 (Figures 1B–1D; Movie S1). Pore opening and closing always reversed after changing the applied voltage, and neither protein instability nor electroporation through the lipid bilayer were observed (Figures S1E–S1H and S3A–S3E). Pore opening occurred from various intermediate conformations, however, with different opening propensities in the order of $IC_{out} < IC_{crystal} < < IC_{int} < IC_{cen}$. For IC_{out} and $IC_{crystal}$, channel opening was never or only once observed (0 out of 4 [IC_{out}] or 1 out of 5 [$IC_{crystal}$, at +1.6 V] simulations) within ~400 ns for each (Figures S2D and S2E). In contrast, such transitions were regularly seen for IC_{cen} and IC_{int} (20 out of 20 [IC_{cen}, at 1.3–1.6 V] or 4 out of 4 [IC_{int}, −1.6 V] simulations) (Figure 1B). To further analyze the conformational changes underlying channel opening and to relate them with translocation of Glt_{Ph}, we performed an additional PCA on all data, including the previously used set of OFC and IFC trajectories, the translocation simulations and all simulations of intermediates under membrane voltages. In addition to EV1—which remained unchanged compared with the first PCA and represents translocation—we found that conformational changes along the fourth eigenvector (EV4) correlated with the onset and ending of anion permeation (Figures S3C–S3E). We plotted the position taken up by the trajectories in the principal component space, as defined by eigenvectors EV1 and EV4, which describe conformational changes attributed to translocation and anion channel gating, respectively (Figure 1E). Although originating from different intermediate states, open channel conformations ChC_{cen} and ChC_{int} had RMSDs approaching 1.0 Å with similar overall structures and will be treated as a single conformation (ChC) (Figures 1E and S3F–S3H).

Formation of the anion conduction pore at the interface between the transport and trimerization domains is accompanied by extensive hydration of this region and the creation of a continuous water bridge spanning the membrane (Figure 2A). In each of our simulations, this process was reversible with channel closure preceded by complete dewetting. Water entry is promoted by both positive and negative potentials with voltage-independent water occupancy between −400 and +400 mV (Figure 2B). The hydrophobic environment of this region (see below) is expected to represent a barrier to anion permeation that can be dynamically lowered by the entry of water molecules. Wetting of the rather hydrophobic interface region might compensate for the energetic cost of breaking hydrophobic interactions between the surfaces of the trimerization and transport domains during the conformational change that broadens the interface. Therefore, we suggest that channel opening and closing is mediated by a combination of steric and hydrophobic gating, as has been demonstrated for some other ion channels (Jensen et al., 2012; Vaitheeswaran et al., 2004).

Structural Determinants of Glt_{Ph} Anion Permeation

The Glt_{Ph} anion conduction pathway has a distorted hourglass shape, with large extra- and intracellular entrance cavities that

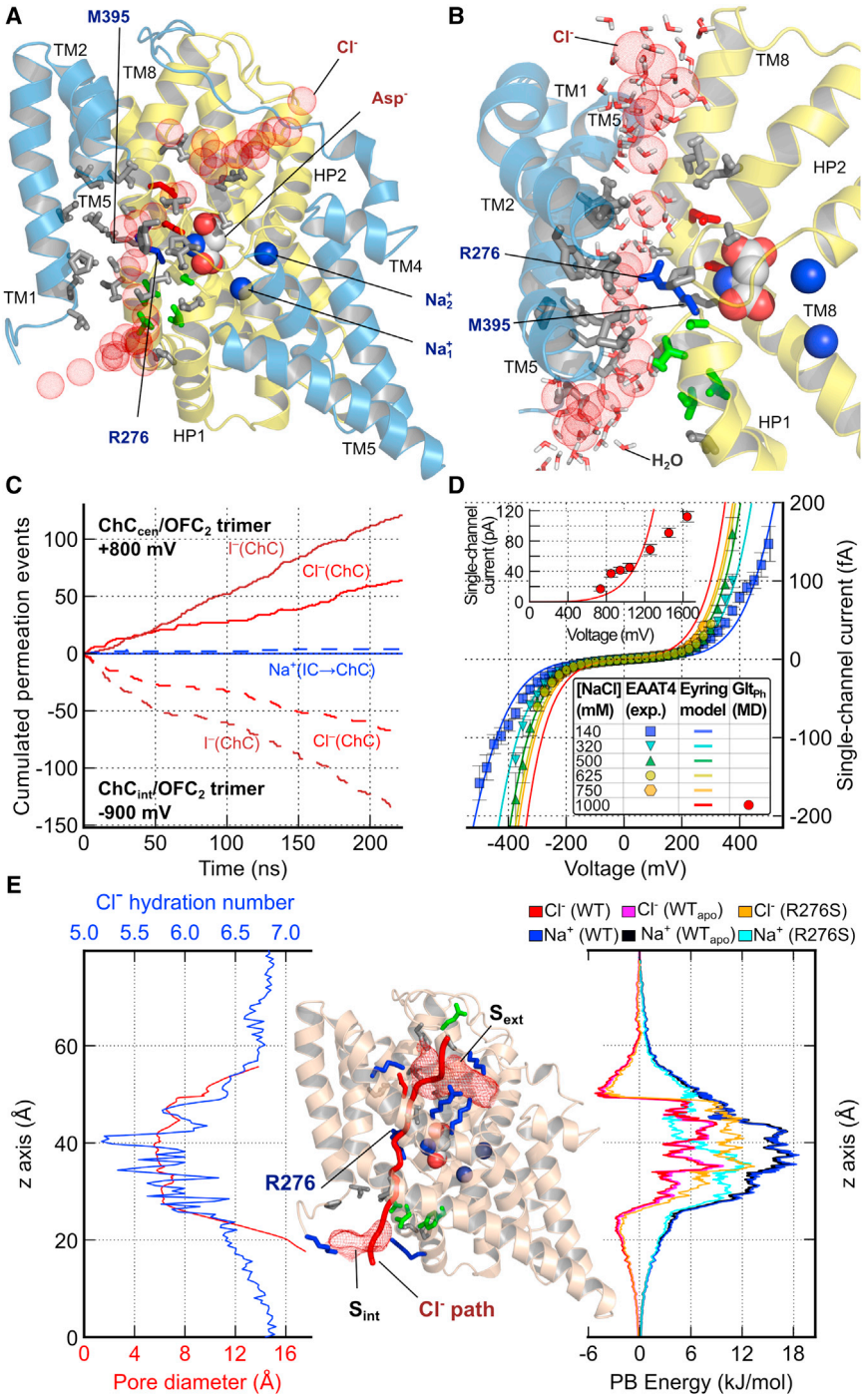

Figure 3. Structural Determinants of Glt_{Ph} Anion Permeation

(A) Cartoon representation of a ChC_{cen} monomer (light blue, trimerization domain; yellow, transport domain) in side view from the subunit interface, with pore-lining side chains shown as sticks (blue, positive; red, negative; green, polar; gray, apolar). TM2 and TM5 are partially omitted for clarity. Red spheres represent snapshots of a single permeating Cl^- ion.

(B) Close-up of the permeation pathway from the TM4–TM5 loop. Coloring as in (A), including representative water molecules found in the inner hydration shell of permeating Cl^- ions.

(C) Count of Cl^- and I^- permeation events through ChC_{cen} and ChC_{int} at +800 and −900 mV (dashed lines), respectively.

(D) EAAT4 current voltage plots for various symmetrical [NaCl]. Single-channel currents were determined by multiplying whole-cell Cl^- currents recorded 1 ms after the voltage jump (means ± SE, n > 10 for each condition) by the ratio of experimentally measured unitary current (Figure 6B) and mean current amplitudes (n = 12) at +150 mV in 140 mM NO_3^-. The experimental data (symbols) were globally fitted using a three-binding site Eyring rate model (lines; Extended Experimental Procedures). The inset displays Glt_{Ph} unitary current amplitudes (red symbols) from MD simulations using 1 M NaCl and the extrapolation of the experimental data to these conditions by the Eyring model (red line).

(E) Pore profile of anion hydration, pore diameter, and Poisson-Boltzmann energies for Na^+ and Cl^- of WT and R276S and of WT Glt_{Ph} in an apo state, i.e., after removal of aspartate and Na^+ ions (in ChC_{cen}). Hydration numbers are the average number of hydrogens within the first Cl^- hydration shell. Cl^- isodensity meshes around ChC_{cen} (4.2σ) illustrate two Cl^--binding sites at the channel entrances, denoted S_{ext} and S_{int}.

See also Figure S4.

narrow to a more constricted conduction path almost perpendicular to the membrane (Figures 1D, 3A, and 3B; Movie S1). Pore-forming residues are highly conserved between Glt_{Ph} and mammalian EAATs (Figure S4). This level of conservation is consistent with the functional similarity between Glt_{Ph} (Ryan and Mindell, 2007) and EAAT anion channels (Melzer et al., 2003; Wadiche and Kavanaugh, 1998) and accounts for similar unitary current amplitudes among EAATs with large glutamate transport and small anion current components and those with predominant anion conductance (Schneider et al., 2014; Torres-Salazar and Fahlke, 2007). Most side chains lining the pore center are hydrophobic, except for R276, which protrudes from the tip of HP1 into the Cl^- density (Figures 3A and 3B). EAATs lack a positive side chain at the position corresponding to R276, but contain arginine at positions homologous to M395 of Glt_{Ph} (Ryan et al., 2010) (Figure S4). MD simulations of the R276S-M395R Glt_{Ph} mutant (see below) showed that both the arginine in the "EAAT position" and R276 project their side chain toward the same location, resulting in conservation of the positive charge at this site in the tertiary structure of EAATs and Glt_{Ph} (Figures 3A and 3B).

Starting from the ChC_{cen} conformation, we simulated anion permeation at reduced voltages of ±~800 mV and observed

perfect anion selectivity (Figure 3C). In 1 M NaCl, our simulations yielded single-channel anion currents of 42.4 ± 6.3 pA (∼+800 mV) or 51.4 ± 6.7 pA (∼−900 mV). These voltages and salt concentration are too high to permit direct experimental verification of the conductances. We measured EAAT4 anion currents at 140–750 mM NaCl and at voltages up to 500 mV (Figure 3D) to extrapolate the voltage dependence of EAAT4 unitary anion currents to the MD conditions. Comparing these experimental EAAT4 and simulated Glt_{Ph} current-voltage relationships demonstrated that simulations reproduce the experimental unitary current amplitudes within the same order of magnitude (Figure 3D, inset). Substitution of Cl^- by I^- in the simulations resulted in significantly higher anion currents of 95.0 ± 5.4 pA (∼+800 mV) or of 97.1 ± 10 pA (∼−900 mV; Figure 3C); however, the transport substrate aspartate did not permeate within 200 ns at concentrations of ∼500 mM. Simulated permeation properties thus closely resemble the functional characteristics of mammalian EAATs (Melzer et al., 2003; Wadiche and Kavanaugh, 1998).

The electrostatic Poisson-Boltzmann energy profile for moving an ion along the channel axis displays much higher energy barriers for Na^+ than for Cl^- (Figure 3E). Energy wells at both entrances with high Cl^- densities represent Cl^- binding sites, denoted S_{ext} and S_{int}. The critical role of R276 in anion selectivity is demonstrated by the convergence of Na^+ and Cl^- energy barriers upon removal of the positive charge in R276S Glt_{Ph} (Figure 3E). Energy profiles are identical in both the presence and absence of bound aspartate/Na^+ at their binding sites (Figure 3E). Simulated ion permeation through this apo state revealed similar Cl^- permeation rates along the same permeation pathway (data not shown), consistent with the experimentally determined unitary conductances of EAATs being indistinguishable in the presence and absence of substrate (Kovermann et al., 2010). The conduction pathway is rather wide with a minimum diameter of 5.6 Å, such that anions can permeate in a partially hydrated state, and Cl^--H_{water} coordination numbers show only a small decrease from 6.8 in bulk solution to 5.2 in the Glt_{Ph} channel center (Figure 3E).

Tryptophan-Scanning Mutagenesis Reveals Direct Interactions of Predicted Pore-Forming Residues with Permeant Anions

We used a combination of tryptophan-scanning mutagenesis and iodide quenching (Vázquez-Ibar et al., 2004) to test whether permeating anions come into close contact with amino acid side chains projecting into the proposed anion conduction pathway. I^- readily permeates through Glt_{Ph} and EAAT anion channels and is therefore expected to come into close proximity to residues forming the permeation pathway. Because I^- can reduce tryptophan fluorescence via direct interactions, i.e., collisional quenching (Lakowicz, 2006), iodide quenching of tryptophan fluorescence is a suitable method to experimentally verify the simulated Glt_{Ph} anion permeation pathway. As Glt_{Ph} lacks endogenous tryptophans, we generated single-tryptophan mutants by substituting 13 residues that protrude from the trimerization domain into the interface region of Glt_{Ph} ChC_{cen} (Figure 4A). To avoid interference with substrate binding, we did not insert tryptophan residues into the transport domain. With the exception of S65W, I^- reduced fluorescence in all Glt_{Ph} mutants in a concentration-dependent manner. Figure 4B shows the spectral properties of V51W and S65W Glt_{Ph} in detergent micelles and their modification at various [I^-]. The identical concentration dependences of the fluorescence lifetimes and intensities indicate that I^- quenches tryptophan fluorescence via a collisional mechanism (Figure 4B, inset).

Figure 4A maps the relative quenching (F_o/F) at [I^-] = 350 mM of the tested tryptophan residues on the ChC_{cen} structure. These data demonstrate the high iodide accessibility of residues close to the proposed anion permeation pathway, which is reduced with increasing distance. Linear concentration dependences of F_0/F in Stern-Volmer plots are expected for proteins with a single tryptophan, which adopt only one conformation. The observed deviations from linearity indicate that tryptophan-substituted Glt_{Ph} mutants assume multiple conformations that differ in I^- accessibility (Figure 4C). These findings support the notion that tryptophan-substituted Glt_{Ph} mutants exhibit similar degrees of conformational heterogeneity to wild-type (WT) Glt_{Ph}.

Figure 4D shows plots of the calculated anion accessibilities in simulations of different conformations compared with experimentally observed fluorescence quenching. Most residues are accessible in multiple conformations. However, there are three residues—W50, W54 (projecting directly into the anion pore), and W62 (at a more peripheral location)—with rather exclusive anion accessibility in ChC (Figures 4D and S5; see the Extended Experimental Procedures for details on the calculation of anion accessibilities from the simulations). For these constructs, a modified Stern-Volmer analysis was used to determine the fraction of fluorescence quenchable by I^- to be ∼20% (Figures S5A and S5B). Because different protein conformations could exhibit different quantum yields of the inserted tryptophan, this value is not always identical to the probability of the protein assuming this accessible conformation. However, these data indicate that Glt_{Ph} can assume the anion-conducting channel conformation ChC even in the absence of an applied voltage and that this conformation is sufficiently stable to permit I^- collisions with side chains that project into the anion conduction pathway.

Mutations of Pore-Forming Residues Affect Unitary Anion Current Amplitudes and Anion/Cation Permeability Ratios

To provide further verification of the predicted anion permeation pathway, we compared the effects of amino acid exchanges on simulated and experimental permeation properties. We chose experimental measures corresponding to parameters obtained from MD simulations: these included the single-channel conductance and the anion/cation selectivity of the anion channel. In contrast, macroscopic current amplitudes alone, e.g., from whole-cell recordings, do not permit a distinction to be made between mutations that alter the anion permeation rate or those that affect the probability of assuming an open anion channel state and therefore preclude a direct comparison with simulation results. Because of difficulties in cellular expression systems, high-resolution electrophysiological recordings of Glt_{Ph} are not yet feasible. Assays that were developed to describe Glt_{Ph} anion conductance (Ryan and Mindell, 2007) only provide information

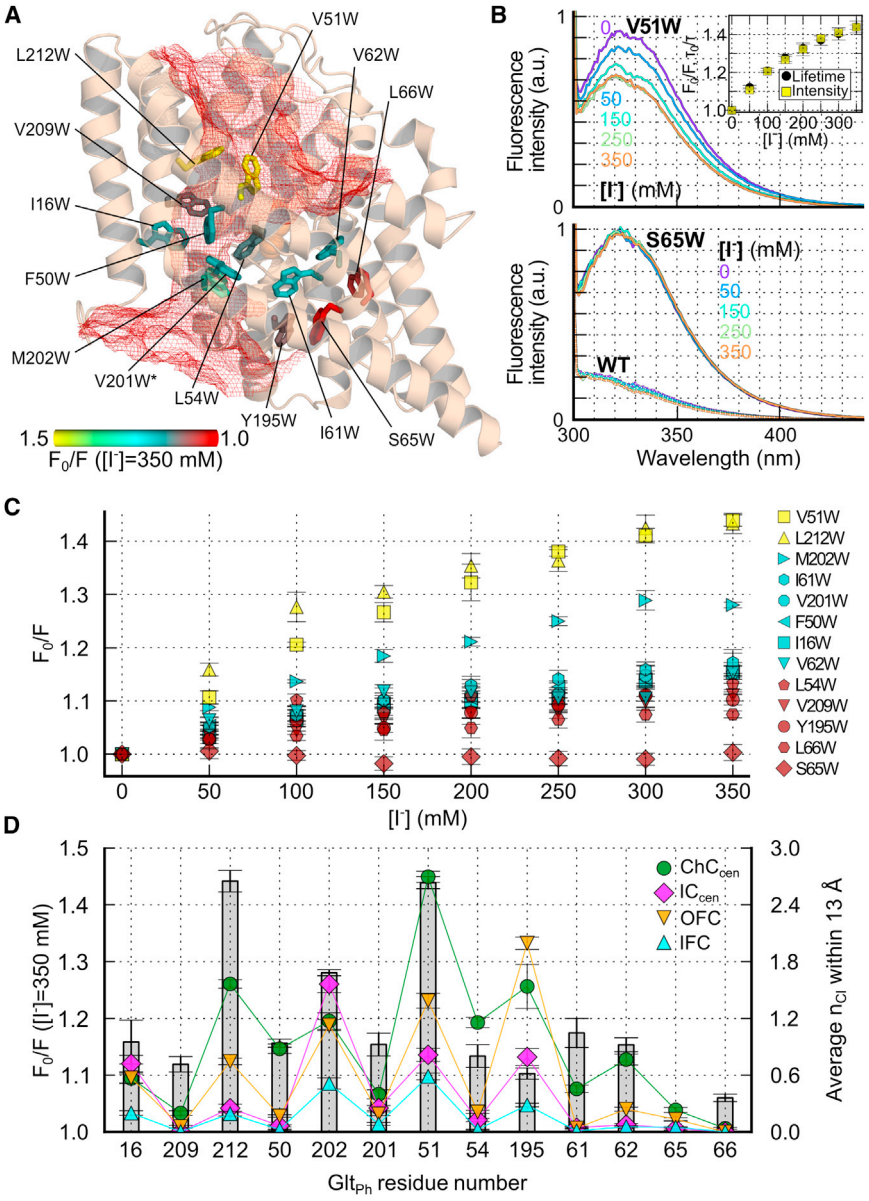

Figure 4. Tryptophan Fluorescence Quenching by Iodide in Glt_{Ph}

(A) Overview of Glt_{Ph} single-tryptophan insertions (ChC_{cen} in side view). Side chains are color-coded according to the reduction in fluorescence intensity at 350 mM [I^-] (F_0 is the intensity in the absence of I^-; n ≥ 5 for each). Red mesh represents the Cl^- density observed in MD (Figure 1D).

(B) Representative fluorescence spectra of WT, V51W, and S65W Glt_{Ph} at various [I^-]. The inset shows the comparable concentration dependence of V51W fluorescence lifetimes and intensities in a Stern-Volmer plot, indicating a collisional quenching mechanism.

(C) Stern-Volmer plots for all tryptophan mutants (means ± SE; n ≥ 5 for each).

(D) Comparison of fluorescence quenching (gray bars; n ≥ 5 for each) with MD-predicted anion accessibilities of side chains in various conformations (the different symbols show the average number of Cl^- ions ± SD within 13 Å of the side chains). Residue numbers on the abscissa are ordered according to their positions in the membrane plane shown in (A).

See also Figure S5.

We initially screened for mutations that affect pore properties in silico. Pore-forming residues were identified by a geometrical criterion (within a distance <6.9 Å to the pore center defined by R276). We excluded only a few residues that are located within the transport domain and known to be crucial for substrate binding (e.g., residues in HP2 to prevent interference with substrate binding). We generated 29 Glt_{Ph} pore mutants in silico, including S65 and I61, which are close to a recently discussed alternative location of the anion channel (see below) and subjected them to MD simulations. We identified side-chain substitutions that increase or decrease unitary conductances (I16E/K, L20E, F50L/K/D, V51D, L54D, I61D, A205D, R276S/D) or modify the anion/cation selectivity (F50D, A205D, R276S) (Figure 5). We then performed whole-cell patch-clamp recordings of 33 EAAT2/EAAT4 mutants (Figure S6). Because most mutations also affected anion channel gating (Figure S6), a direct comparison of whole-cell currents and MD data was not feasible. However, ten EAAT4 mutants exhibited sufficient time- and voltage-dependent gating to allow single-channel conductances to be determined using nonstationary noise analysis (Figure 6). Four charge-altering mutations, L20E, I16K, I16E and I61D, increased or decreased the simulated Cl^- permeation rate of Glt_{Ph} to a similar extent as alterations in experimental single-channel conductance caused by the homologous EAAT4 mutations. For four Glt_{Ph} mutants, V12E, I16W, and S65A, experimental and simulated unitary conductances were unaltered (Figure 6B). Interestingly, I16E—located in the intracellular part of the

about macroscopic anion currents through an ensemble of multiple Glt_{Ph} transporters. Because the functional properties of Glt_{Ph} (Ryan and Mindell, 2007) and EAAT anion channels are very similar (Melzer et al., 2003; Wadiche and Kavanaugh, 1998) and the pore-lining residues are highly conserved (Figure S4), it is reasonable to assume that the proposed Glt_{Ph} anion permeation pathway is also responsible for EAAT anion conduction. We therefore compared the effects of in silico mutagenesis on simulated Glt_{Ph} anion conductance and anion/cation selectivity with experimental data on mammalian EAAT2/EAAT4. Single-channel recordings have not yet been possible for these transporters, but unitary current amplitudes can be determined by noise analysis of whole-cell current recordings, and anion/cation selectivities can be obtained through reversal potential measurements at various ionic conditions (Melzer et al., 2003).

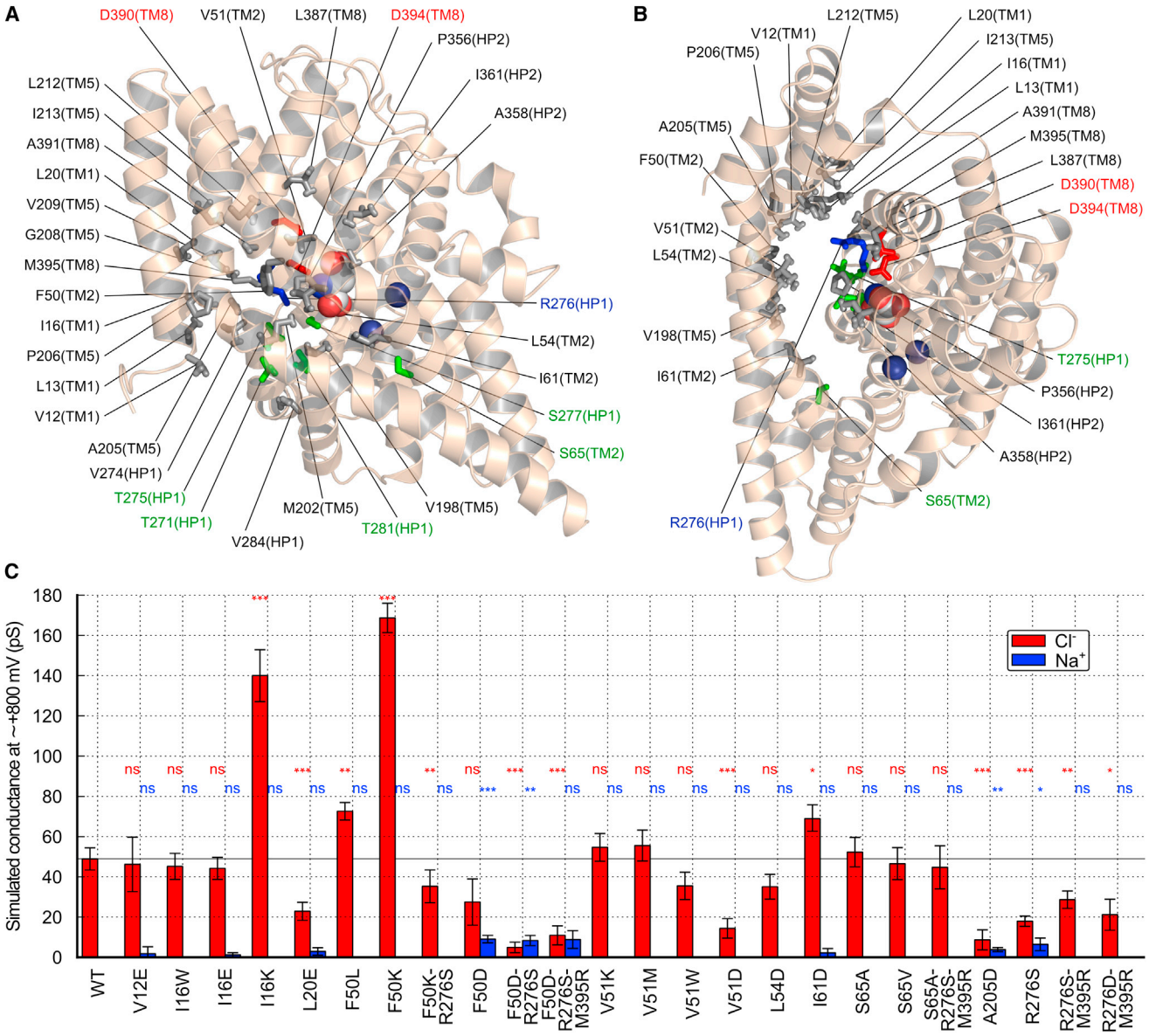

Figure 5. MD Screening of Pore-Lining Residues Predicts Mutations that Affect Anion Conductance and Anion/Cation Selectivity

(A and B) Stick representations of pore-lining residues in side view (A) or top view (B) and colored as in Figure 3A, including detailed Glt_{Ph} residue number labels. (C) Summary of simulated Na^+/Cl^- conductances for various Glt_{Ph} mutants (ChC_{cen}; means ± SD; MD times range from 120 to 500 ns for each mutant) at ~+800 mV.

Glt_{Ph} anion conduction pathway—selectively reduced outward fluxes of anions in a valve-like manner, as demonstrated by outward current rectification in the I16E Glt_{Ph} and homologous T59E EAAT4 mutants. In contrast, for the neighboring residue V12, which is closer to the bulk solution and further from the pore center than I16 (Figure 5A), conversion to glutamate did not affect unitary conductances in Glt_{Ph} or in F55E EAAT4. We furthermore found four "semiconserved" side chains that are conserved within mammalian EAATs but differ in Glt_{Ph}: the aforementioned R276 residue (the corresponding EAAT arginine is located at the M395 position in Glt_{Ph}), F50 (L in EAATs), and M94 (V in EAATs; Figure S4). We constructed Glt_{Ph} and EAAT4 mutants to reverse these evolutionary exchanges and observed reciprocal effects on conductance, as would be expected if direct interactions exist between these side chains and permeating anions (Figure 6C).

The simulated Glt_{Ph} mutants F50D, A205D, and R276S exhibited Na^+ permeation along the same path as Cl^- (Figures 7A and 7C). Because some of the corresponding EAAT4 mutations prevented their functional expression in cells, homologous mutations were introduced into EAAT2, a transporter with unitary current properties similar to those of EAAT4 (Schneider et al., 2014).

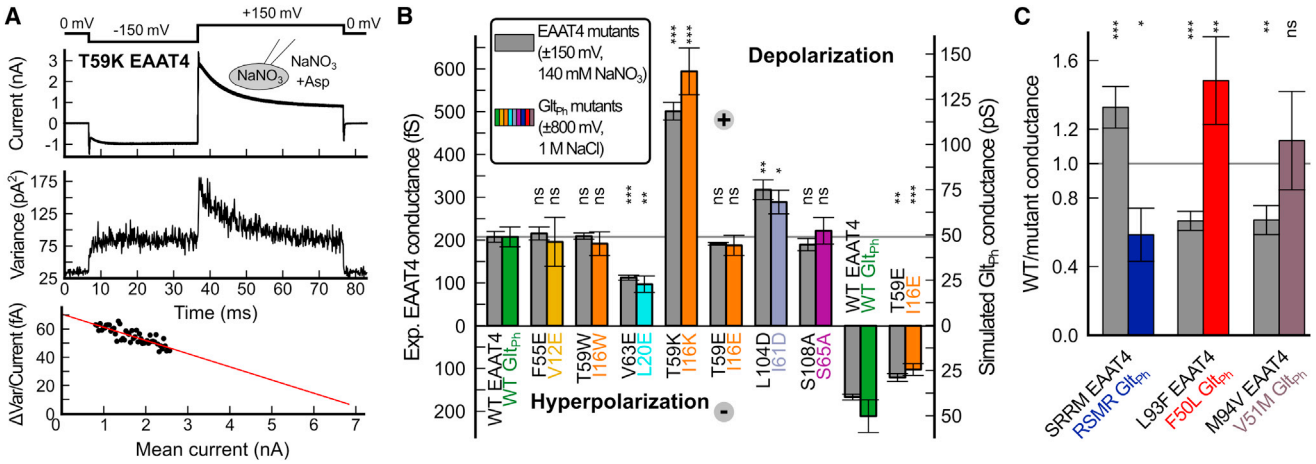

Figure 6. Mutations of Pore-Forming Residues Modify Experimental EAAT4 Anion Conductances and Anion/Cation Selectivity

(A) Representative nonstationary noise analysis of T59K EAAT4, showing current responses to 300 repeated voltage jumps (top) and the resulting current variances (middle). Bottom, linearly transformed current-variance plot (background noise at 0 mV was subtracted from the total variance). Red line shows a linear fit.

(B) Experimental EAAT4 (gray; from whole-cell recordings and nonstationary noise analysis; means ± SE; n = 6–9) and simulated Glt_{Ph} unitary conductances of WT and homologous mutants (in color; means ± SD). Ordinates were scaled to show experimental WT EAAT4 conductances at +150 mV and simulated WT Glt_{Ph} conductances at +800 mV at the same level (gray line).

(C) Changes in experimental EAAT4 (n = 6–8) and simulated Glt_{Ph} unitary conductance upon substitution of residues that are conserved in EAATs, but not in Glt_{Ph} (Figure S4).

See also Figures S6 and S7 and Table S1.

Varying the external [Na^+] led to changes in ion current reversal potentials in cells expressing L85D, S288D, and R476M EAAT2, indicating that EAAT2 mutants represent unselective channels with varying degrees of relative cation selectivity (Figure 7B). In these experiments, coupled glutamate transport, which would additionally affect the reversal potential, was abolished by using a K^+-free intracellular solution.

The effect of these negative charge mutations was site-specific as demonstrated by experiments and simulations with A362D EAAT2 and the corresponding R276D-M395R Glt_{Ph}. A362 in EAAT2 is homologous to R276 in Glt_{Ph}, whose positively charged side chain is crucial for anion selectivity (Figure 3). To achieve the electrostatic potential in Glt_{Ph} to be similarly modified as in A362 EAAT2, we inserted an arginine at the "EAAT position" M395, in addition to the R276D mutation (Figures 3A and S4). R276D-M395R Glt_{Ph} and A362D EAAT2 exhibited perfect Cl^- selectivity in both simulations and experiments, indicating that anion selectivity is only impaired by the insertion of negatively charged side chains at specific positions (Figures 5 and 7).

The Novel Anion Channel Conformation Enables a Reinterpretation of Previous Functional Data and Is Compatible with Published Crosslinking Results

Prior to our work, the structural basis of EAAT/Glt_{Ph} anion conduction was unknown. However, because mutations around S65 were reported to affect anion permeation of both Glt_{Ph} (Ryan and Mindell, 2007) and EAAT1 (Cater et al., 2014; Ryan et al., 2004), and because crystallographic data (Verdon and Boudker, 2012) suggested the existence of an aqueous cavity in $IC_{crystal}$, it has been hypothesized that anions permeate along a pathway that we will refer to as "S65 path" (Figure S7A). As yet, no other EAAT anion permeation pathway has been proposed.

We performed MD simulations and experimental approaches to test whether anion permeation along the "S65 path" might contribute to EAAT/Glt_{Ph} anion conduction. MD simulations demonstrated water access but no Cl^- density along the "S65 path" in ChC (Figure S7A). Pore searching algorithms (see the Extended Experimental Procedures) did not identify any additional candidate anion pore in the S65 region. Mutations of S65 did not affect anion conductance in MD simulations (Figure 5). In our fluorescence assay, S65W Glt_{Ph} fluorescence was not quenched by iodide (Figure 4). Whereas the homologous S108V EAAT4 mutant was mostly retained in intracellular compartments, S108A EAAT4 was robustly expressed on the surface of mammalian cells, with resulting current amplitudes comparable with those of WT EAAT4. S108A EAAT4 exhibited altered anion channel gating but unaltered unitary current amplitudes (Figures 6B and S6). These results indicate that mutations of S65/S108 do not affect the single-channel conductance itself but instead alter the channel open probability, i.e., the rates of reactions leading to the open anion channel.

We generated three additional EAAT4 mutants (V101D, L104D, and N297D) with negatively charged side chains projecting into the "S65 path." Mutant channels exhibited altered voltage- and glutamate-dependent gating but were still glutamate sensitive and cation impermeable (Figures S6B, S6C, S7A, and S7B). One mutation in this region, I61D Glt_{Ph}/L104D EAAT4, even increased anion permeation rates in both simulations and experiments (Figures 5 and 6B). Because this residue does not directly line the Cl^- permeation pathway, which remained unchanged upon I61D substitution, and because the introduction of a negative charge increases anion conductance, we deduce that this mutation indirectly affects the anion channel function. We conclude that the mutated amino acids surrounding

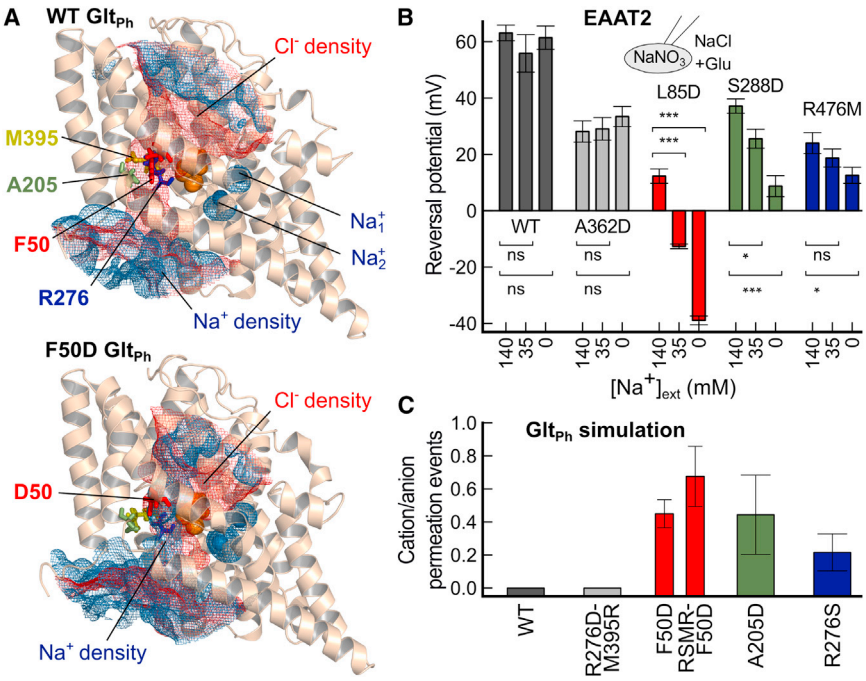

Figure 7. Conversion of the EAAT2 Anion Pore into a Cation-Conducting Channel

(A) Cl^- (red) and Na^+ (blue) distributions (σ = 0.2) around WT and F50D Glt_{Ph}. Residues described in (B) and (C) are shown as sticks.

(B) Variations in current reversal potentials with external [Na^+] demonstrate the cation permeability of L85D EAAT2—homologous to F50D Glt_{Ph}—S288D, and R476M (but not of WT and A362D) EAAT2 anion channels (means ± SE; n = 6–13 for each).

(C) Ratio of simulated cation/anion permeation events for WT and corresponding Glt_{Ph} mutants (means ± SD; RSMR, R276S-M395R), colored according to (B). The F50D mutant was tested with the arginine at position 276 (WT) and in the context of the EAAT arginine position (RSMR mutation).

See also Figures S6 and S7 and Table S1.

S65 in Glt_{Ph} do not line the EAAT anion pore, although they do influence the conformational changes underlying the probability of the channel being open.

A recent study demonstrated that crosslinking a substituted cysteine within the transport domain to another in the trimerization domain abolishes EAAT3 glutamate transport but does not abrogate substrate-dependent anion conductance (Shabaneh et al., 2014). The authors concluded that, starting from OFC, a limited inward movement of the transport domain is sufficient for formation of an anion conducting conformation. Cysteines were inserted at positions corresponding to residues 216 and 391 in Glt_{Ph}. These residues are in close proximity in OFC, IC_{out}, and $IC_{crystal}$. Because MD simulations demonstrated a pronounced increase in the V216–A391 C_α distance to >7 Å during transmembrane translocation and channel opening (Figure S7C), this disulfide link might prevent transitions into the IC_{cen}, IC_{int}, ChC, and IFC states. To evaluate the effects of this disulfide bridge on the conformational changes underlying anion channel opening, we performed simulations on an intermediate conformation of our translocation trajectory that is located at the most central position along the translocation axis (to increase the likelihood of pore opening) but maintains a distance between these two residues of $\leq$7 Å (Figures 1 and S7C). The crosslinkage was modeled by a distance restraint on the two C_α atoms within monomers (Figures S7C and S7D). Simulations of the V216–A391 crosslinked Glt_{Ph} model showed that this disulfide link limits the lateral movement of the transport domain but permits sufficient conformational flexibility for pore opening and anion permeation along the identified anion conduction pore (Figures S7E and S7F). The experimental effects of this crosslink on transport and anion currents in EAAT3 (Shabaneh et al., 2014) are therefore fully consistent with the Glt_{Ph} anion permeation pathway presented here.

DISCUSSION

EAAT glutamate transporters are prototypical dual function proteins that operate as both secondary active transporters and anion-selective ion channels. Whereas the key structural features of secondary active glutamate transport have been established (Akyuz et al., 2013; Crisman et al., 2009; Reyes et al., 2009; Shrivastava et al., 2008), structural and mechanistic details of anion permeation have been hitherto unknown. In this study, we used a combination of computational and experimental approaches to determine how this class of transporters mediates anion permeation through an aqueous conduction pathway. MD simulations identified an open channel conformation of Glt_{Ph} that was consistently formed from various ICs by the lateral movement of the transport domain (Figure 1). Opening of the interface between the transport and trimerization domains is followed by voltage-promoted water entry (Figure 2) and the formation of an anion-selective conduction pathway (Figure 3). We verified the predictions of our simulations by fluorescence spectroscopy and functional studies using mutant transporters. Fluorescence quenching experiments demonstrated that tryptophan residues substituted at positions that project into the predicted conduction pathway come into close contact with permeating anions (Figure 4). Moreover, substitution of pore-forming residues had comparable experimental effects on the two key characteristics of an anion-selective conduction pathway, i.e., anion/cation selectivity and ion permeation rates, as predicted by simulations (Figures 5, 6, and 7). These data indicate that pore-forming residues identified through simulations are indeed the major determinants of anion permeation and selectivity in both Glt_{Ph} and EAATs. Moreover, they demonstrate that this anion conduction pathway is conserved throughout the glutamate transporter family. Our data thus clarify how a class of secondary active transporters can function as anion-selective channels that are gated by transitions in the transport cycle.

The ion conduction pathway reported herein accounts for all known functional properties of EAAT/Glt_{Ph} anion channels.

Simulations reveal unitary current amplitudes and ion selectivities (Figures 3C and 3D) that resemble experimental results (Melzer et al., 2003; Wadiche and Kavanaugh, 1998). The calculated minimum pore diameter of Glt_{Ph} is ~5.6 Å (Figure 3E), which perfectly fits the predicted minimum pore diameter of >5 Å based on anion substitution experiments on EAAT1 anion channels (Wadiche and Kavanaugh, 1998). Rapid substrate application experiments have shown that EAAT anion channel activation is delayed compared with glutamate translocation (Grewer et al., 2000). These findings indicate that anion-conducting states existing "outside" the glutamate uptake cycle can be explained by channel opening as a branching reaction from ICs (Figure 1). Simulations predict voltage independence of anion channel opening within the physiological voltage range (Figure 2B). This result explains the experimental observation that the voltage- and substrate dependence of EAAT anion channels are tightly linked to transitions within the transport cycle (Bergles et al., 2002; Machtens et al., 2011a). Simulated anion permeation is unchanged in both the presence and absence of bound substrate (Figure 3E), as expected from the experimental unitary conductances being indistinguishable in the presence and absence of glutamate (Kovermann et al., 2010). Because anion channel opening is tightly linked to translocation of the transport domain, our results indicate that transport substrates increase EAAT anion currents by promoting intermediate states. Distinct EAAT isoforms differ strongly in the relative amplitudes of their transport and anion currents (Fairman et al., 1995; Mim et al., 2005). However, analysis of unitary current amplitudes revealed similar single-channel amplitudes (Schneider et al., 2014; Torres-Salazar and Fahlke, 2007). The high degree of conservation of pore-forming residues (Figure S4) is consistent with the similarities in anion channel unitary current amplitudes and selectivity of different transporter isoforms. Lastly, the novel anion conducting conformation can account for all published mutagenesis and crosslinking results on EAAT anion conduction (Ryan et al., 2004; Shabaneh et al., 2014).

The "S65 path" (Figure S7) is the only location of the anion channel that has been discussed in recent years. We could not find any indication for a direct contribution of this region to anion permeation. Our simulations show that the "S65 path" is hydrated in ChC, thereby suggesting that S65 and adjacent residues could be involved in facilitating the opening of the transport/trimerization domain interface instead. We thus speculate that the "S65 path" may modulate formation of the ChC conformation, which provides an explanation for the impact of mutations in this region on anion channel function (Cater et al., 2014; Ryan and Mindell, 2007; Ryan et al., 2004).

The positive electrostatic potential necessary for perfect anion selectivity of EAAT/Glt_{Ph} anion channels is provided by a single positively charged side chain, R276. Surprisingly, during evolution, this arginine has moved from the tip of HP1 in Glt_{Ph} to TM8 in EAATs, while retaining a similar side chain position in the tertiary structure. In Glt_{Ph}, as well as in EAATs, this arginine has been implicated in binding amino acid substrates, as well as binding Na^+ and K^+ (Ryan et al., 2010; Verdon et al., 2014). Unitary anion conductance is not affected by aspartate (Figure 3), indicating that the interaction of R276 with transport substrates does not modify its effect on anion conduction and selectivity.

The tight linkage between anion channel gating and glutamate transport in EAAT/Glt_{Ph} was previously explained by assuming that certain states of the transport cycle are anion conducting (Bergles et al., 2002). Because Glt_{Ph} structures did not exhibit an open pore with dimensions that might account for the experimentally observed anion conduction properties, it was recently suggested that additional yet to be defined ICs that occur during translocation might be anion conducting (Cater et al., 2014). We have now demonstrated that intermediate transport conformations are nonconducting and that EAAT/Glt_{Ph} anion channel opening transitions require the lateral movement of the glutamate transport domain together with pore hydration from intermediates. Anion channel opening is therefore not part of the transport cycle, but instead is achieved via a branching conformational change. This design permits rapid transition through the full transport cycle without anion channel opening. Furthermore, it allows certain EAAT isoforms to function as effective transporters, with low anion channel open probabilities, and other isoforms to have low transport rates but high occupations of the anion channel mode.

The unique mechanism of EAAT anion channel gating results in neuronal or glial anion conductances that follow changes in substrate concentrations and thus allow feedback control of glutamate release (Wersinger et al., 2006) or modification of GABAergic postsynaptic currents by glutamatergic signals (Winter et al., 2012). Moreover, it explains why isoform-specific variations in glutamate transport by EAATs result in the formation of anion channels that preferentially open or close within their physiological voltage range (Schneider et al., 2014). Recently, gain-of-function mutations in genes encoding EAAT anion channels have been linked to pathological neuronal excitability and cell-volume regulation (Winter et al., 2012). EAAT anion channel activity is also enhanced under conditions of increased synaptic glutamate concentration and may thus contribute to the clinical symptoms associated with brain ischemia or certain neurodegenerative diseases. The structural and mechanistic data presented here might help in the design of EAAT anion channel modulators and thus open therapeutic avenues to correct the cellular defects linked to these pathological conditions.

EXPERIMENTAL PROCEDURES

Molecular Simulations

MD simulations of Glt_{Ph}—bound by a negatively charged aspartate and two Na^+ ions—in outward-facing (OFC; Protein Data Bank [PDB] ID code 2NWX), inward-facing (IFC; PDB ID code 3KBC), and various intermediate conformations (including $IC_{crystal}$; PDB ID code 3V8G) were performed using GROMACS 4.5 (Hess et al., 2008). Based on our OFC and IFC simulation trajectories, we obtained intermediates IC_{int}, IC_{cen}, and IC_{out} from the crystallographic structures of OFC and IFC using essential dynamics sampling simulations (Amadei et al., 1996). Proteins were inserted and equilibrated in a double dimyristoyl phosphatidylcholine bilayer surrounded by a 1 M NaCl aqueous solution and were subjected to various membrane potentials using the computational electrophysiology scheme described recently (Kutzner et al., 2011).

Molecular Biology

Mutant constructs of Glt_{Ph}, human EAAT4, and rat EAAT2 were generated using the QuikChange Site-Directed Mutagenesis Kit (Agilent Technologies) and verified by restriction analysis and DNA sequencing.

Fluorescence Spectroscopy

Fluorescence emission spectra of single-tryptophan Glt_{Ph} mutants in n-dodecyl-β-D-maltoside micelles in the presence of saturating [Na^+] and [Asp^-] at various [I^-] were recorded after excitation at 295 nm. Fluorescence lifetimes were determined through time-correlated single-photon counting.

Electrophysiology

Heterologous expression and whole-cell patch-clamp recordings of EAAT2 and EAAT4 were performed as described previously (Machtens et al., 2011a). Unitary conductances were determined by nonstationary noise analysis of current responses to 300 repetitive voltage jumps to ±150 mV using 140 mM NO_3^- as main anion and 1 mM aspartate as substrate to enhance voltage-dependent gating of the channel.

Statistics

Asterisks indicate the level of statistical significance derived from a two-tailed t test (*** $p < 0.001$; ** $p < 0.01$; * $p < 0.05$; ns, $p \geq 0.05$; see Table S1).

SUPPLEMENTAL INFORMATION

Supplemental Information includes Extended Experimental Procedures, seven figures, one table, and one movie and can be found with this article online at http://dx.doi.org/10.1016/j.cell.2014.12.035.

AUTHOR CONTRIBUTIONS

J.-P.M. and Ch.F. designed the research; J.-P.M. carried out MD simulations; J.-P.M., P.K., and B.B. generated mutant DNA constructs; J.-P.M., D.K., and A.L. performed patch-clamp recordings; C.L. and D.E. conducted fluorescence spectroscopy measurements; J.-P.M. and D.E. analyzed data; B.L.d.G., R.B., and U.Z. advised on the setup and analysis of MD simulations; and J.-P.M., D.E., R.B., B.L.d.G., and Ch.F. prepared the figures and wrote the paper.

ACKNOWLEDGMENTS

These studies were supported by the Deutsche Forschungsgemeinschaft (FA301/9 to Ch.F.; SFB803 to B.L.d.G. and R.B.). The authors gratefully acknowledge the computing time granted on the supercomputer JUROPA at Jülich Supercomputing Centre (JSC) and on the HLRN-II supercomputer of the North-German Supercomputing Alliance (HLRN). We thank A. Alekov, K. Benndorf, H. Grubmüller, and P. Hidalgo for critically reading the manuscript; T. Becher, R.E. Guzman, P. Kovermann, G. Stölting, B. Wilhelm, T. Gensch, I. Weyand, D. Köpfer, D. Wojciechowski, and D.J. Slotboom for helpful discussions; and T. Wassmann for preliminary simulations.

Received: May 23, 2014
Revised: August 27, 2014
Accepted: December 19, 2014
Published: January 29, 2015

REFERENCES

Akyuz, N., Altman, R.B., Blanchard, S.C., and Boudker, O. (2013). Transport dynamics in a glutamate transporter homologue. Nature *502*, 114–118.

Amadei, A., Linssen, A.B.M., de Groot, B.L., van Aalten, D.M.F., and Berendsen, H.J.C. (1996). An efficient method for sampling the essential subspace of proteins. J. Biomol. Struct. Dyn. *13*, 615–625.

Bergles, D.E., Tzingounis, A.V., and Jahr, C.E. (2002). Comparison of coupled and uncoupled currents during glutamate uptake by GLT-1 transporters. J. Neurosci. *22*, 10153–10162.

Boudker, O., Ryan, R.M., Yernool, D., Shimamoto, K., and Gouaux, E. (2007). Coupling substrate and ion binding to extracellular gate of a sodium-dependent aspartate transporter. Nature *445*, 387–393.

Cater, R.J., Vandenberg, R.J., and Ryan, R.M. (2014). The domain interface of the human glutamate transporter EAAT1 mediates chloride permeation. Biophys. J. *107*, 621–629.

Crisman, T.J., Qu, S., Kanner, B.I., and Forrest, L.R. (2009). Inward-facing conformation of glutamate transporters as revealed by their inverted-topology structural repeats. Proc. Natl. Acad. Sci. USA *106*, 20752–20757.

Erkens, G.B., Hänelt, I., Goudsmits, J.M., Slotboom, D.J., and van Oijen, A.M. (2013). Unsynchronised subunit motion in single trimeric sodium-coupled aspartate transporters. Nature *502*, 119–123.

Fairman, W.A., Vandenberg, R.J., Arriza, J.L., Kavanaugh, M.P., and Amara, S.G. (1995). An excitatory amino-acid transporter with properties of a ligand-gated chloride channel. Nature *375*, 599–603.

Grewer, C., Watzke, N., Wiessner, M., and Rauen, T. (2000). Glutamate translocation of the neuronal glutamate transporter EAAC1 occurs within milliseconds. Proc. Natl. Acad. Sci. USA *97*, 9706–9711.

Grewer, C., Balani, P., Weidenfeller, C., Bartusel, T., Tao, Z., and Rauen, T. (2005). Individual subunits of the glutamate transporter EAAC1 homotrimer function independently of each other. Biochemistry *44*, 11913–11923.

Groeneveld, M., and Slotboom, D.J. (2010). Na^+:aspartate coupling stoichiometry in the glutamate transporter homologue Glt_{Ph}. Biochemistry *49*, 3511–3513.

Hess, B., Kutzner, C., van der Spoel, D., and Lindahl, E. (2008). GROMACS 4: algorithms for highly efficient, load-balanced, and scalable molecular simulation. J. Chem. Theory Comput. *4*, 435–447.

Jensen, M.O., Jogini, V., Borhani, D.W., Leffler, A.E., Dror, R.O., and Shaw, D.E. (2012). Mechanism of voltage gating in potassium channels. Science *336*, 229–233.

Kanner, B.I., and Sharon, I. (1978). Active transport of L-glutamate by membrane vesicles isolated from rat brain. Biochemistry *17*, 3949–3953.

Kovermann, P., Machtens, J.P., Ewers, D., and Fahlke, C. (2010). A conserved aspartate determines pore properties of anion channels associated with excitatory amino acid transporter 4 (EAAT4). J. Biol. Chem. *285*, 23676–23686.

Kutzner, C., Grubmüller, H., de Groot, B.L., and Zachariae, U. (2011). Computational electrophysiology: the molecular dynamics of ion channel permeation and selectivity in atomistic detail. Biophys. J. *101*, 809–817.

Lakowicz, J.R. (2006). Principles of fluorescence spectroscopy. In Principles of Fluorescence Spectroscopy, P.H. Lakowicz, ed. (New York: Springer), pp. 529–575.

Machtens, J.P., Kovermann, P., and Fahlke, C. (2011a). Substrate-dependent gating of anion channels associated with excitatory amino acid transporter 4. J. Biol. Chem. *286*, 23780–23788.

Melzer, N., Biela, A., and Fahlke, C. (2003). Glutamate modifies ion conduction and voltage-dependent gating of excitatory amino acid transporter-associated anion channels. J. Biol. Chem. *278*, 50112–50119.

Mim, C., Balani, P., Rauen, T., and Grewer, C. (2005). The glutamate transporter subtypes EAAT4 and EAATs 1-3 transport glutamate with dramatically different kinetics and voltage dependence but share a common uptake mechanism. J. Gen. Physiol. *126*, 571–589.

Otis, T.S., and Kavanaugh, M.P. (2000). Isolation of current components and partial reaction cycles in the glial glutamate transporter EAAT2. J. Neurosci. *20*, 2749–2757.

Picaud, S.A., Larsson, H.P., Grant, G.B., Lecar, H., and Werblin, F.S. (1995). Glutamate-gated chloride channel with glutamate-transporter-like properties in cone photoreceptors of the tiger salamander. J. Neurophysiol. *74*, 1760–1771.

Reyes, N., Ginter, C., and Boudker, O. (2009). Transport mechanism of a bacterial homologue of glutamate transporters. Nature *462*, 880–885.

Ryan, R.M., and Mindell, J.A. (2007). The uncoupled chloride conductance of a bacterial glutamate transporter homolog. Nat. Struct. Mol. Biol. *14*, 365–371.

Ryan, R.M., Mitrovic, A.D., and Vandenberg, R.J. (2004). The chloride permeation pathway of a glutamate transporter and its proximity to the glutamate translocation pathway. J. Biol. Chem. *279*, 20742–20751.

Ryan, R.M., Kortt, N.C., Sirivanta, T., and Vandenberg, R.J. (2010). The position of an arginine residue influences substrate affinity and K^+ coupling in the human glutamate transporter, EAAT1. J. Neurochem. *114*, 565–575.

Schneider, N., Cordeiro, S., Machtens, J.P., Braams, S., Rauen, T., and Fahlke, C. (2014). Functional properties of the retinal glutamate transporters GLT-1c and EAAT5. J. Biol. Chem. *289*, 1815–1824.

Shabaneh, M., Rosental, N., and Kanner, B.I. (2014). Disulfide cross-linking of transport and trimerization domains of a neuronal glutamate transporter restricts the role of the substrate to the gating of the anion conductance. J. Biol. Chem. *289*, 11175–11182.

Shrivastava, I.H., Jiang, J., Amara, S.G., and Bahar, I. (2008). Time-resolved mechanism of extracellular gate opening and substrate binding in a glutamate transporter. J. Biol. Chem. *283*, 28680–28690.

Torres-Salazar, D., and Fahlke, C. (2007). Neuronal glutamate transporters vary in substrate transport rate but not in unitary anion channel conductance. J. Biol. Chem. *282*, 34719–34726.

Vaitheeswaran, S., Rasaiah, J.C., and Hummer, G. (2004). Electric field and temperature effects on water in the narrow nonpolar pores of carbon nanotubes. J. Chem. Phys. *121*, 7955–7965.

Vázquez-Ibar, J.L., Guan, L., Weinglass, A.B., Verner, G., Gordillo, R., and Kaback, H.R. (2004). Sugar recognition by the lactose permease of Escherichia coli. J. Biol. Chem. *279*, 49214–49221.

Verdon, G., and Boudker, O. (2012). Crystal structure of an asymmetric trimer of a bacterial glutamate transporter homolog. Nat. Struct. Mol. Biol. *19*, 355–357.

Verdon, G., Oh, S., Serio, R.N., and Boudker, O. (2014). Coupled ion binding and structural transitions along the transport cycle of glutamate transporters. eLife *3*, e02283.

Wadiche, J.I., and Kavanaugh, M.P. (1998). Macroscopic and microscopic properties of a cloned glutamate transporter/chloride channel. J. Neurosci. *18*, 7650–7661.

Wersinger, E., Schwab, Y., Sahel, J.A., Rendon, A., Pow, D.V., Picaud, S., and Roux, M.J. (2006). The glutamate transporter EAAT5 works as a presynaptic receptor in mouse rod bipolar cells. J. Physiol. *577*, 221–234.

Winter, N., Kovermann, P., and Fahlke, C. (2012). A point mutation associated with episodic ataxia 6 increases glutamate transporter anion currents. Brain *135*, 3416–3425.

Yernool, D., Boudker, O., Jin, Y., and Gouaux, E. (2004). Structure of a glutamate transporter homologue from Pyrococcus horikoshii. Nature *431*, 811–818.

EXTENDED EXPERIMENTAL PROCEDURES

Molecular Dynamics Simulations

Molecular dynamics (MD) simulations were carried out using GROMACS 4.5 (Hess et al., 2008). The simulation box (~147·147·107 Å^3) contained two equilibrated and fully hydrated dimyristoyl phosphatidylcholine (DMPC) lipid bilayers, surrounded by a 1 M NaCl aqueous solution. Glt_{Ph} trimers were embedded into each membrane using g_membed (Wolf et al., 2010). Before production runs, the systems were equilibrated in the absence of membrane voltage by 40 ns simulation with position restraints on the protein heavy atoms, followed by an additional 20 ns with backbone-only position restraints. The AMBER99SB-ILDN force field was used for the protein (Lindorff-Larsen et al., 2010). Parameters for ions and lipids were derived from (Berger et al., 1997; Joung and Cheatham, 2008). Water was modeled using the SPC/E water model. Water-bond distances and angles were constrained using SETTLE (Miyamoto and Kollman, 1992), and all other bonds were constrained using LINCS (Hess, 2008). A constant temperature was maintained by coupling protein and non-protein separately to a heat bath at 310 K using the Nosé-Hoover algorithm (Hoover, 1985). A constant pressure of 1 bar was maintained by employing the semi-isotropic Parrinello-Rahman barostat (Nosé and Klein, 1983; Parrinello and Rahman, 1981). Using virtual sites for hydrogen atoms enabled simulation to be performed with 4 fs time steps. Crystallographic structures used for MD simulations were the homotrimeric, substrate-bound conformations of Glt_{Ph} in outward- and inward-facing conformations (OFC_3 and IFC_3, respectively) and the asymmetric trimer $IC_{crystal}/IFC_2$ (PDB ID codes 2NWX, 3KBC, and 3V8G). Glt_{Ph} monomers were simulated with substrates bound as defined by the crystal structures (Boudker et al., 2007), i.e., with negatively charged aspartate and Na^+_1 and Na^+_2, if not stated otherwise. All structures of Glt_{Ph} mutants were generated using MODELLER (v. 9.10) (Eswar et al., 2007).

Computational Electrophysiology

Transmembrane potential gradients in MD simulations were generated by introducing a charge difference between the aqueous compartments on both sides of the bilayer in a double-membrane system as described recently (Kutzner et al., 2011) (Figure S1A). Due to periodic boundary conditions, atoms can freely diffuse over the simulation system borders into replicated copies of themselves, thus making it difficult to establish a charge imbalance across a lipid membrane for setting up a potential gradient. However, the use of a double-membrane system creates two separate compartments, and therefore makes it possible to maintain an ion concentration gradient across each membrane. During MD simulation, the ion numbers in both compartments were controlled by an algorithm, such that a slight charge gradient was applied across the membrane (Kutzner et al., 2011). The resulting membrane potential can be calculated by double-integration of the charge distribution using the Poisson equation. In each of the two parallel lipid membranes, a Glt_{Ph} trimer was embedded in the same orientation and the difference in Cl^- numbers between both compartments was controlled to yield voltage differences from ± 600 mV to ± 1.6 V across the membrane (i.e., one bilayer was depolarized and the other hyperpolarized, with respect to the cytoplasmic side of the protein). In order to observe sufficient anion permeation events in individual simulations of 100–500 ns, 1 M NaCl (or NaI, if stated) was used. The ChC_{cen} conformation that formed at ± 1.6 V was used as starting conformation for all simulations, since anion channel opening (IC_{cen}–ChC_{cen} transition) did not always occur spontaneously within simulation times of up to 1 μs at lower voltages. The absence of membrane or protein structure instabilities or of electroporation through the lipid bilayer justified the use of supraphysiological voltages to sample sufficient permeation events at reasonable computational cost (Figures S1–S2). The open channel conformations (ChCs) generated in these simulations were then set to a voltage of ± 800 mV, resulting in strict anion selectivity for WT Glt_{Ph} (Figures 3, 5, 6, and 7). The majority of the further simulations were performed at ± 800 mV (Figures 5, 6, and 7). For the results from Figure 3D, additional voltages between +750 mV and +1.5 V were applied. Electroporation through the lipid membrane was only observed in test simulations at > 1.8 V.

Essential Dynamics Sampling

Essential dynamics sampling permits the accelerated simulation of conformational transitions along predefined reaction coordinates (Amadei et al., 1996). We employed this technique for the OFC–IFC conformational transition of Glt_{Ph} to identify intermediate structures (e.g., IC_{out}, IC_{cen} and IC_{int}). As EAAT subunits function independently of each other (Erkens et al., 2013; Grewer et al., 2005; Koch et al., 2007; Leary et al., 2007), this transition was simulated in a single monomer (Stolzenberg et al., 2012), leaving the other two monomers unaffected in the OFC. We first performed a Cartesian principal component analysis (PCA) on the monomeric trajectories of all OFC and IFC simulations. The calculated 1st eigenvector (EV1) represented transmembrane translocation, i.e., movement of the transport domain (harboring the substrate-binding sites) along the membrane normal. We applied a constraint force along EV1 to one monomer (monomer 1) of an OFC trimer, leaving the other two unchanged in the OFC (Figures S1C and S1D). With a step size of 5·10^{-6} Å, monomer 1 approached the IFC conformation within 333 ns at a minimum root-mean-square deviation (RMSD) of 2.0 Å (Figures S1C and S1D). This close structural similarity supports the simulated reaction pathway because the algorithm only controls progression along the one-dimensional reaction coordinate, leaving all other degrees of freedom untouched (Amadei et al., 1996).

All errors given in the analysis of MD simulations were estimated by subdividing the trajectories of each simulation into six parts of equal length and calculating the SE. The given RMSD values refer to backbone atoms only. All molecular representations were made using PyMOL (Schrödinger, 2010). Ion distributions around the protein were estimated from time-averaged densities and represented as meshes of X σ over the average. The pore diameter profile (Figure 3E) was calculated using the Voronoi diagram-based pore searching algorithm implemented in MOLE1.2 (Petrek et al., 2007); this program was also used to identify other possible permeation pathways. However, no other ion pore except the one presented here (Figure 1) was found, in particular no pathway was

detected along the "S65 path" (Figure S7A). Electrostatic energies were calculated as Poisson-Boltzmann energies using APBS (Baker et al., 2001) in 150 mM NaCl aqueous solution with a dielectric constant of 4.0 for the protein and 78.5 for the surrounding medium (Figure 3E).

Fluorescence Spectroscopy

Expression constructs were generated using a QuikChange Site-Directed Mutagenesis Kit (Agilent Technologies, Waldbronn, Germany) from a pBAD24 vector containing the wild-type (WT) Glt_{Ph} sequence (GenBank ID code BA000001.2) with a C-terminal 8×-histidine tag (kindly provided by Dr. Eric Gouaux, Oregon, USA). WT and mutant Glt_{Ph} were expressed in *Escherichia coli* Top10 cells (Invitrogen) and purified as described recently (Ewers et al., 2013). If necessary, proteins were concentrated using ultrafiltration columns (Millipore, MA, USA) prior to experiments. To ensure complete equilibration with measuring conditions, proteins were subjected to four successive purification steps with disposable desalting columns (GE Healthcare, Chalfont St. Giles, UK), equilibrated in 20 mM Tris (pH 7.4) containing 500 mM CholineCl, 1 mM *n*-dodecyl-β-D-maltoside (DDM), followed by equilibration in fluorescence background buffer (20 mM Tris [pH 7.4] 1 M Na_2SO_4, 1 mM DDM, 100 μM L-aspartate). During all fluorescence measurements, the sum of the optical densities of the measured solutions at excitation and emission wavelengths did not exceed 0.05.

Fluorescence spectra were determined using a Fluorolog-3 spectrofluorometer (HORIBA Jobin Yvon, Unterhaching, Germany) and a Quantamaster 4 spectrofluorometer (Photon Technology, NJ, USA). Excitation and emission slits were set to band passes of 2–3 nm. Photomultiplier photon counts following excitation at 295 nm were corrected for instrumental wavelength dependence and excitation intensity. Emissions of $[I^-]$ containing solutions were collected in the front face configuration. Glt_{Ph} fluorescence intensities were obtained by subtracting the background signal from a 10 mm cuvette from the signal obtained from the same cuvette containing Glt_{Ph}. For all tryptophan-substituted Glt_{Ph}, emission spectra peaked at around 320 nm. This value is shifted toward smaller wavelengths compared with values obtained for tryptophan residues that are fully accessible to water, most likely since tryptophans are not exposed to solution in all possible Glt_{Ph} conformations. We modified $[I^-]$ by replacing appropriate amounts of the background buffer with 20 mM Tris, at pH 7.4, 2 M NaI, 1 mM DDM, 100 μM L-aspartate and 500 μM $K_2S_2O_3$. The fluorescence intensity was integrated from 303 to 440 nm or from 304 to 440 nm, depending on the amount of scattered light, as judged from visual inspection.

For a single-tryptophan protein that adopts just one tryptophan-accessible conformation, the $[I^-]$ dependence of quenching is given by

$$\frac{F}{F_0} = \frac{1}{1 + K_{SV}[I^-]}, \qquad \text{(Equation 1)}$$

or in its inverted form, i.e., the classical Stern–Volmer equation,

$$\frac{F_0}{F} = 1 + K_{SV}[I^-], \qquad \text{(Equation 2)}$$

with F_0 and F being the fluorescence intensities in the absence or in the presence of quencher $[I^-]$ and K_{SV} the Stern-Volmer constant (Lakowicz, 2006). A plot of F_0/F versus $[I^-]$ (Equation 2) provides a linear relationship for proteins with a single tryptophan and one tryptophan-accessible protein conformation (Rasmussen et al., 2010).

For all tested tryptophan-substituted Glt_{Ph}, Stern-Volmer plots showed deviations from linearity, as expected for proteins which can assume multiple conformations with different tryptophan accessibilities (Figures 4B and 4C). The experimentally observed $[I^-]$ dependence of quenching could be described with the modified Stern-Volmer equation. For this equation, it is assumed that the inserted tryptophan is only accessible in one conformation, but inaccessible in all other conformations. In the absence of iodide, the iodide-accessible conformation exhibits a fluorescence amplitude of F_{0a}, and all other non-accessible conformations together F_{0b} (Lehrer, 1971).

$$F = \frac{F_{0a}}{1 + K_{SV}[I^-]} + F_{0b}. \qquad \text{(Equation 3)}$$

Using the additional parameter f_a,

$$f_a = \frac{F_{0a}}{F_{0a} + F_{0b}} = \frac{F_{0a}}{F_0}, \qquad \text{(Equation 4)}$$

which corresponds to the fraction of the fluorescence signal that is accessible to quencher, Equation 1 can be transformed to:

$$\frac{F}{F_0} = \frac{f_a}{1 + K_{SV}[I^-]} + 1 - f_a. \qquad \text{(Equation 5)}$$

Thus, at high $[I^-]$, F/F_0 approaches $1-f_a$.

To predict the conformation-dependent I^- accessibilities of the various inserted tryptophan residues, we analyzed the average number of anions around the center-of-mass (COM) of the different side chains of WT Glt_{Ph} in MD simulations (Figure 4D). The use of the WT trajectories might underestimate the real anion accessibility because the tryptophan side chain has a higher volume than those of other amino acids. In addition, substituted tryptophans might exhibit different side chain orientations that could also affect their accessibility to anions. We addressed these possible limitations by using a distance threshold of 13 Å to the COMs to compensate for the error introduced by the analysis of the WT, i.e., non-tryptophan, side chains (Lakowicz, 2006) and furthermore analyzed the I^- accessibility around the respective tryptophan side chains in simulations of the mutants with tryptophan substitutions that were supposed to be exclusively accessible in ChC_{cen} (Figure 4D). The comparative analysis of both approaches demonstrated that W50, W54, and W62 are exclusively I^- accessible in the ChC conformation (Figure S5C).

We fitted Equation 5 to all quenching data of tryptophan-substituted Glt_{Ph} proteins (Figure S5). For F50W, L54W, and V62W, the obtained f_a values provide the relative fluorescence that is accessible to the quencher in the ChC conformation (Figure 4D). For all other mutants, f_a provides a weighted mean for different I^- accessible conformations. We decided not to present the K_{SV} values obtained from these fits. For most tryptophan substitutions, these parameters represent weighted averages of Stern–Volmer constants in different conformations, which do not provide quantitative information about pore formation and side chain accessibilities that could be compared with the simulations.

For measurements of fluorescence lifetime quenching (Figure 4B, inset), tryptophan excited-state lifetimes were measured using a Fluorolog-3 spectrofluorometer equipped with a DeltaDiode 295 with 5 μM Glt_{Ph} protein in a 5 mm cuvette. The pulsed excitation light with a repetition rate of 20 MHz was passed through a 298HT-05 band pass interference filter (L.O.T. Oriel, Darmstadt, Germany), resulting in an intensity peak at 297 nm. The emission was selected using a HQ385/80 band pass interference filter (L.O.T. Oriel). Polarizers on the excitation and emission sides were set to magic angle conditions. Time-correlated single photon counting was done using a SP-630 module (Becker & Hickl, Berlin, Germany) connected to a cooled R7400U-based (Hamamatsu Photonics, Hamamatsu, Japan) detector module (TBX-05C, HORIBA Jobin Yvon), which was directly attached to the sample chamber. Experimental photon distributions were fitted by iterative reconvolution with distributions obtained from a diluted LUDOX AM-30 solution with omission of the emission filter (instrument response function), using FluoFit software (PICOQUANT, Berlin, Germany).

The applied models correspond to sums of exponential functions according to

$$F(t) = \sum_i \alpha_i \cdot e^{\frac{-t}{\tau_i}}, \qquad \text{(Equation 6)}$$

with lifetime components τ_i and pre-exponential factors α_i. An additional component accounted for the contribution of scattered light. Homogeneous distribution of the residuals around zero, together with a χ^2 value near to 1, without further improvement by more complex models, served as selection criteria for the appropriate fit. Relative intensity contributions of lifetime components were calculated according to

$$f_i = a_i \cdot \tau_i \Big/ \sum_i a_i \cdot \tau_i, \qquad \text{(Equation 7)}$$

and average lifetime values were determined from

$$\langle \tau \rangle = \sum_i f_i \cdot \tau_i. \qquad \text{(Equation 8)}$$

Functional Characterization of WT and Mutant EAATs in Mammalian Cells

Rat EAAT4 (GenBank ID code XM_008765182.1) and human EAAT2 (GenBank ID code AY066021.1) were expressed as fluorescent fusion proteins by transient transfection of HEK293T cells, as described previously (Leinenweber et al., 2011; Machtens et al., 2011a; Melzer et al., 2003). Point mutations were introduced using PCR-based strategies or a QuikChange Site-Directed Mutagenesis Kit (Figure S5). All constructs were verified by restriction analysis and DNA sequencing. For each construct, two independent recombinants from the same transformation were examined and shown to exhibit indistinguishable functional properties.

Standard whole-cell patch-clamp recordings were performed using an Axopatch 200B amplifier (Molecular Devices, Sunnyvale, CA). Borosilicate pipettes were pulled with resistances between 1.0 and 1.5 MΩ, and voltage errors were reduced by compensating 80%–90% of the series resistance by an analog procedure and excluding cells with current amplitudes higher than 12 nA from analysis. Currents were low-pass filtered at 10 kHz and digitized at 50 kHz using a Bessel low-pass filter and a Digidata 1322A AD/DA converter (Molecular Devices). Since EAAT anion channels prefer large or polyatomic (SCN^-, NO_3^-, I^-) to smaller inorganic (e.g., Cl^-) anions, we used NO_3^- as the main anion instead of Cl^- to increase EAAT anion currents in the majority of our experiments (Machtens et al., 2011a; Melzer et al., 2003; Wadiche and Kavanaugh, 1998). To prevent electrogenic substrate transport and directly measure anion currents, we used K^+-free internal solutions containing 115 mM $NaNO_3$, 2 mM $MgCl_2$, 5 mM EGTA and 10 mM HEPES. For most experiments, bath solutions contained 140 mM $NaNO_3$, 1 mM L-glutamic acid or L-aspartic acid, 4 mM KCl, 2 mM $CaCl_2$, 1 mM $MgCl_2$, 5 mM HEPES and 5 mM tetraethylammonium chloride. For the determination of single-channel conductances (Figure 6), aspartate was used instead of glutamate because it increased the time- and voltage-dependent gating of EAAT4 anion channels,

thereby facilitating noise analysis (see below) (Heinemann and Conti, 1992; Machtens et al., 2011b; Melzer et al., 2003). To study the anion concentration dependence of EAAT4 anion currents (Figure 3D) we used extracellular solutions in which [NaCl] was increased to 320, 500, 625 or 750 mM, and intracellular solutions with [NaCl] being 295, 475, 600 or 725 mM.

For experiments designed to test the cation permeability of EAAT2 anion channel mutants, we used external Cl^- instead of NO_3^- (using the same pipette solution). Under these conditions, cells expressing EAAT2 exhibited a positive anion reversal potential, such that cation-conducting mutants led to prominent reversal potential decreases upon reduction of the external Na^+ concentration, with choline chloride used as an equimolar substitute for external NaCl (Figures 7 and S7). In all solutions, pH was adjusted to 7.4 with *N*-methyl-glucamine. External and internal agar salt bridges were made from a plastic tube filled with 3 M KCl in 1.5% agar and used to create an electrical connection with the Ag/AgCl electrode. Cells were clamped to 0 mV for at least 2 s between test sweeps.

Data were analyzed using a combination of pClamp10 (Molecular Devices) and self-written python scripts. Current amplitudes were used without any subtraction procedure. Data are given as means ± SE. All statistical evaluations are based on the two-tailed, unpaired, Student's t test (Table S1).

Eyring Rate Model of Anion Permeation through EAAT4

In order to compare experimental EAAT4 unitary Cl^- currents with those from MD simulations of Glt_{Ph}, a permeability model of Cl^- permeation was developed using Eyring rate theory as described in (Hille, 1975). The model features three Cl^- binding sites, which are assumed to be equidistant for simplicity. Moreover, it is assumed that the pore is never simultaneously occupied by more than one Cl^- ion. All these assumptions are well supported by the MD simulations and Poisson-Boltzmann calculations (Figure 3E). The model was optimized against the experimentally determined Cl^- currents at various voltages and concentrations (Figure 3D) using the genetic algorithm as implemented in MATLAB (version 7, The MathWorks, USA). The energy values of the barriers and valleys from the external to the internal side are: 15.4, −2.71, 20.4, 12.7, 20.1, −13.7 and 15.5 (given in RT units; at 20°C; frequency factor: $6.1 \cdot 10^{12}$ s^{-1}). The so-obtained model was then used to extrapolate the experimental data to the conditions of the MD simulations of Glt_{Ph} (Figure 3D, inset).

Nonstationary Noise Analysis

We used noise analysis to determine single-channel currents of WT and mutant EAAT4 anion channels (Figure 6). EAAT4 expression in cells results in Lorentzian noise that originates from the random opening and closing of EAAT4 anion channels (Kovermann et al., 2010; Melzer et al., 2005). The occupancy of open and closed states of an ion channel can be approximated by a binomial distribution. Using the identity

$$I = Nip \qquad \text{(Equation 9)}$$

with *I* being the macroscopic current amplitude, *i* the single-channel current amplitude, *p* the channel open probability and *N* the number of channels, the current variance (σ_N^2) generated by N channels is thus given by

$$\sigma_N^2 = Ni^2p(1-p) + \sigma_{bg}^2 = iI - \frac{I^2}{N} + \sigma_{bg}^2 \qquad \text{(Equation 10)}$$

or after linear transformation (Alekov and Fahlke, 2009)

$$\frac{\sigma_N^2 - \sigma_{bg}^2}{I} = i - \frac{I}{N} \qquad \text{(Equation 11)}$$

with σ_{bg}^2 representing voltage-independent background noise (Hebeisen et al., 2003).

We used non-stationary noise analysis (Heinemann and Conti, 1992) to analyze current amplitudes and variances following a defined voltage step. Cells were held at a 0 mV holding potential and a series of 300 records was obtained by pulsing to +150 mV from a pre-potential of −150 mV, and vice versa. The experimental non-stationary ensemble variance at each time point was calculated from differences in subsequent records to minimize artifacts arising from small linear drifts during the measurement protocol (around 5 min) (Melzer et al., 2003). The variance determined in cells expressing EAAT4 was at least 5 times larger than the background noise at the current reversal potential or in non-transfected cells (Figure 6). For each cell, a variance-mean current plot was generated and single-channel currents were determined by a least-squares fit of Equations 10 or 11 to these data. To further reduce the degrees of freedom of the fit, the background noise measured at the holding potential (0 mV) was subtracted from the total variance in advance. Current artifacts in individual recording sweeps could lead to overestimation of the true current variance. To reduce this potential bias and to identify those "leaky" sweeps, we performed a systematic analysis of such artifacts. We found that exclusion of all difference sweeps with time-averaged current variances that were higher than twice the overall variance of all sweeps resulted in stable and converging fit parameters that were unaffected by the removal of further outliers. We routinely applied this threshold value, which removed 5%–10% of all sweeps (Schneider et al., 2014).

The resulting single-channel currents determined by non-stationary noise analysis in this, as well as in a previous publication (Melzer et al., 2003), differ from our earlier results using stationary noise analysis (Kovermann et al., 2010). For the following two reasons, we are convinced that non-stationary noise analysis provides more accurate results than stationary noise analysis. Stationary noise analysis requires knowledge about the voltage dependence of single-channel amplitudes (i.e., the i–V characteristic) (Kovermann et al., 2010). In our earlier analyses (Kovermann et al., 2010), we assumed that the single-channel current is proportional to the recorded instantaneous macroscopic current amplitude. However, the existence of very fast reactions within the glutamate uptake cycle (Watzke et al., 2001) might result in deviations from this relationship. Moreover, the non-stationary noise protocol determines the true current variance more accurately. In stationary noise analysis, the variance is calculated from individual steady-state current recordings at various voltages within time scales of ~100 ms (Kovermann et al., 2010; Torres-Salazar and Fahlke, 2007). In contrast, non-stationary noise analysis extracts the variance from pre-steady-state currents upon repeated short voltage steps (e.g., ~300 repeats of ~50 ms) to the same voltage over a longer period (e.g., ~5 min). Non-stationary noise analysis thus enables a longer total observation time of the channel noise and better sampling of rare events (slow reactions within the transport cycle) that may not be detected in stationary noise analysis. For example, EAAT4 has a very slow turnover rate of < 3/s (Mim et al., 2005). Therefore, the slowest time constant within the glutamate reaction cycle should be > 333 ms, and important events might be missed during the short records used in stationary noise analysis (Machtens et al., 2011b). Hence, we used non-stationary noise analysis to assess the effects of EAAT4 pore-lining mutants.

SUPPLEMENTAL REFERENCES

Alekov, A.K., and Fahlke, C. (2009). Channel-like slippage modes in the human anion/proton exchanger ClC-4. J. Gen. Physiol. *133*, 485–496.

Baker, N.A., Sept, D., Joseph, S., Holst, M.J., and McCammon, J.A. (2001). Electrostatics of nanosystems: application to microtubules and the ribosome. Proc. Natl. Acad. Sci. USA *98*, 10037–10041.

Berger, O., Edholm, O., and Jähnig, F. (1997). Molecular dynamics simulations of a fluid bilayer of dipalmitoylphosphatidylcholine at full hydration, constant pressure, and constant temperature. Biophys. J. *72*, 2002–2013.

Eswar, N., Webb, B., Marti-Renom, M.A., Madhusudhan, M.S., Eramian, D., Shen, M.Y., Pieper, U., and Sali, A. (2007). Comparative protein structure modeling using MODELLER. Curr. Protoc. Protein Sci. *Chapter 2*, Unit 2.9.

Ewers, D., Becher, T., Machtens, J.P., Weyand, I., and Fahlke, C. (2013). Induced fit substrate binding to an archeal glutamate transporter homologue. Proc. Natl. Acad. Sci. USA *110*, 12486–12491.

Hebeisen, S., Heidtmann, H., Cosmelli, D., Gonzalez, C., Poser, B., Latorre, R., Alvarez, O., and Fahlke, C. (2003). Anion permeation in human ClC-4 channels. Biophys. J. *84*, 2306–2318.

Heinemann, S.H., and Conti, F. (1992). Nonstationary noise analysis and application to patch clamp recordings. Methods Enzymol. *207*, 131–148.

Hess, B. (2008). P-LINCS: a parallel linear constraint solver for molecular simulation. J. Chem. Theory Comput. *4*, 116–122.

Hille, B. (1975). Ionic selectivity, saturation, and block in sodium channels. A four-barrier model. J. Gen. Physiol. *66*, 535–560.

Hoover, W.G. (1985). Canonical dynamics: Equilibrium phase-space distributions. Phys. Rev. A *31*, 1695–1697.

Joung, I.S., and Cheatham, T.E., 3rd. (2008). Determination of alkali and halide monovalent ion parameters for use in explicitly solvated biomolecular simulations. J. Phys. Chem. B *112*, 9020–9041.

Katz, B.A., and Kossiakoff, A. (1986). The crystallographically determined structures of atypical strained disulfides engineered into subtilisin. J. Biol. Chem. *261*, 15480–15485.

Koch, H.P., Brown, R.L., and Larsson, H.P. (2007). The glutamate-activated anion conductance in excitatory amino acid transporters is gated independently by the individual subunits. J. Neurosci. *27*, 2943–2947.

Leary, G.P., Stone, E.F., Holley, D.C., and Kavanaugh, M.P. (2007). The glutamate and chloride permeation pathways are colocalized in individual neuronal glutamate transporter subunits. J. Neurosci. *27*, 2938–2942.

Lehrer, S.S. (1971). Solute perturbation of protein fluorescence. The quenching of the tryptophyl fluorescence of model compounds and of lysozyme by iodide ion. Biochemistry *10*, 3254–3263.

Leinenweber, A., Machtens, J.P., Begemann, B., and Fahlke, C. (2011). Regulation of glial glutamate transporters by C-terminal domains. J. Biol. Chem. *286*, 1927–1937.

Lindorff-Larsen, K., Piana, S., Palmo, K., Maragakis, P., Klepeis, J.L., Dror, R.O., and Shaw, D.E. (2010). Improved side-chain torsion potentials for the Amber ff99SB protein force field. Proteins *78*, 1950–1958.

Machtens, J.P., Fahlke, C., and Kovermann, P. (2011b). Noise analysis to study unitary properties of transporter-associated ion channels. Channels (Austin) *5*, 468–474.

Melzer, N., Torres-Salazar, D., and Fahlke, C. (2005). A dynamic switch between inhibitory and excitatory currents in a neuronal glutamate transporter. Proc. Natl. Acad. Sci. USA *102*, 19214–19218.

Miyamoto, S., and Kollman, P.A. (1992). Settle: An analytical version of the SHAKE and RATTLE algorithm for rigid water models. J. Comput. Chem. *13*, 952–962.

Nosé, S., and Klein, M.L. (1983). Constant pressure molecular dynamics for molecular systems. Mol. Phys. *50*, 1055–1076.

Parrinello, M., and Rahman, A. (1981). Polymorphic transitions in single crystals: A new molecular dynamics method. J. Appl. Phys. *52*, 7182–7190.

Petrek, M., Kosinová, P., Koca, J., and Otyepka, M. (2007). MOLE: a Voronoi diagram-based explorer of molecular channels, pores, and tunnels. Structure *15*, 1357–1363.

Rasmussen, T., Edwards, M.D., Black, S.S., Rasmussen, A., Miller, S., and Booth, I.R. (2010). Tryptophan in the pore of the mechanosensitive channel MscS: assessment of pore conformations by fluorescence spectroscopy. J. Biol. Chem. *285*, 5377–5384.

Schrödinger, L.L.C. (2010). The PyMOL molecular graphics system.

Stolzenberg, S., Khelashvili, G., and Weinstein, H. (2012). Structural intermediates in a model of the substrate translocation path of the bacterial glutamate transporter homologue Glt_{Ph}. J. Phys. Chem. B *116*, 5372–5383.

Watzke, N., Bamberg, E., and Grewer, C. (2001). Early intermediates in the transport cycle of the neuronal excitatory amino acid carrier EAAC1. J. Gen. Physiol. *117*, 547–562.

Wolf, M.G., Hoefling, M., Aponte-Santamaría, C., Grubmüller, H., and Groenhof, G. (2010). g_membed: Efficient insertion of a membrane protein into an equilibrated lipid bilayer with minimal perturbation. J. Comput. Chem. *31*, 2169–2174.

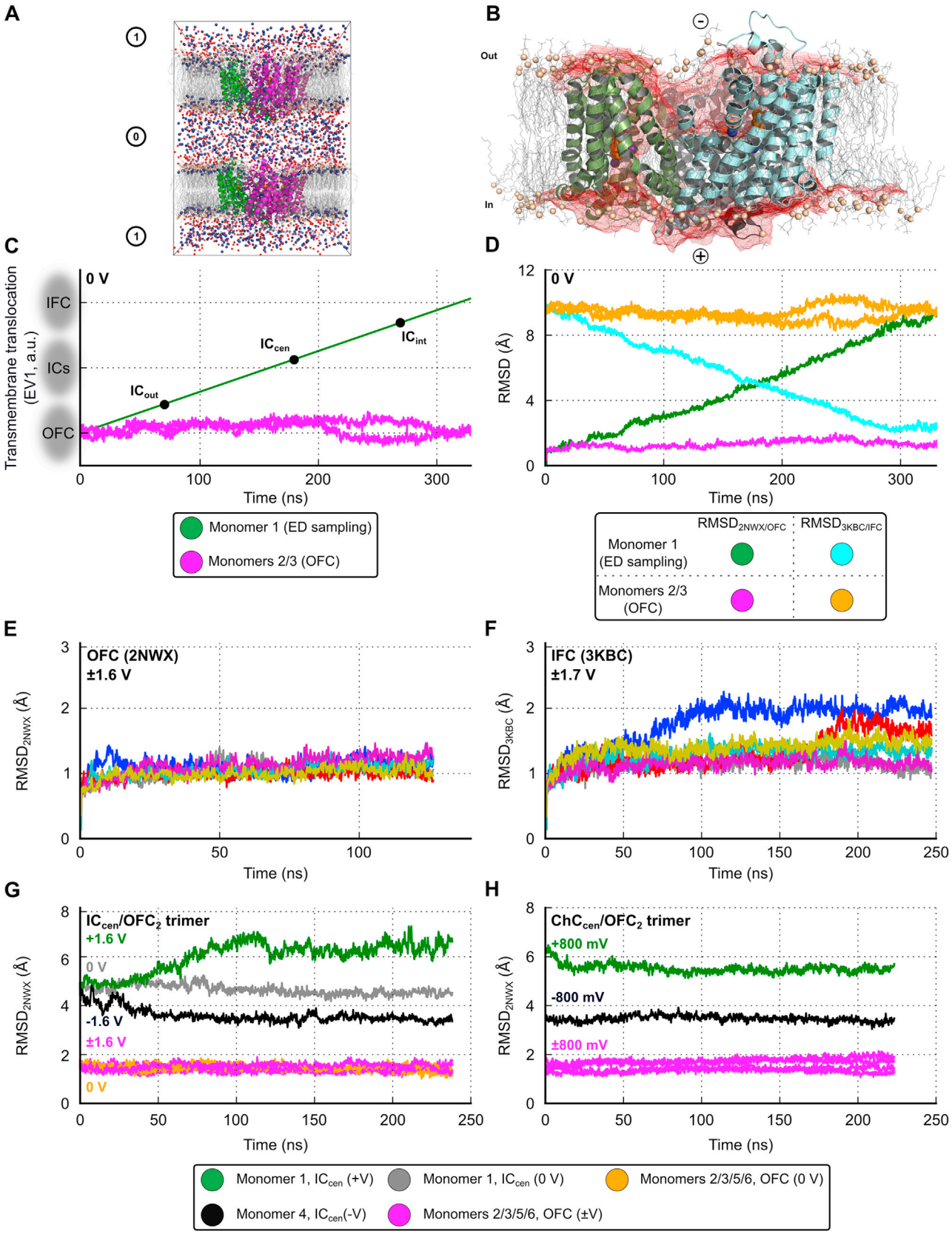

(legend on next page)

Figure S1. The Simulation System for Computational Electrophysiology and Conformational Changes and Stability during Molecular Dynamics Simulations, Related to Figure 1

(A) The use of a double-membrane system creates two separate compartments (0 and 1) and allows the maintenance of a small charge imbalance across the lipid bilayer, despite the presence of periodic boundary conditions.

(B) Cl^- distribution (red isodensity mesh) around an asymmetric IC_{cen}/OFC_2 trimer (side view), derived from essential dynamics (ED) sampling simulations (Figure 1A). For clarity, only the lower half of the system is shown, in which the protein is subjected to +800 mV. If not stated otherwise, Glt_{Ph} monomers were simulated with the substrates bound as defined by the crystal structures, i.e., with negatively charged aspartate and Na^+_1 and Na^+_2. Water molecules and ions in solution have been omitted for clarity; only DMPC lipids around the protein are shown as gray lines and their phosphorus atoms as beige spheres.

(C) Time course of the ED sampling simulation of transmembrane translocation. A membrane-embedded OFC trimer was simulated with ED applied to a single monomer (monomer 1) to ensure transition at constant velocity along an eigenvector (EV1) representing the OFC–IFC isomerization. The other two monomers (monomers 2 and 3) were unaffected. Positions of the snapshots IC_{out}, IC_{cen} and IC_{in}, used in this study, are indicated.

(D) Quantification of the structural changes that occur during ED simulation in terms of the root-mean-square deviation (RMSD) time course with respect to the crystallographic OFC and IFC structures (PDB ID codes 2NWX and 3KBC). During the simulation, monomer 1, to which ED was applied, finally approached the IFC conformation at 2.0 Å. This validates the simulated conformational change because the algorithm only controls progression along the one-dimensional reaction coordinate, leaving all other degrees of freedom untouched.

(E and F) RMSD stability of OFC or IFC trimers at a membrane potential of ± 1.6–1.7 V.

(G) RMSD stability of the IC_{cen}/OFC_2 trimer taken from the ED simulation (C) as a snapshot at 180 ns. The system was subsequently duplicated to obtain a double-membrane setup and set to a membrane potential of ∼ ± 1.6 V. For comparison, the same simulation at 0 V is also shown.

(H) Continuation of the simulation of the conducting conformation (ChC) taken from the previous simulation at +1.6 V at 120 ns (G), which was subsequently set to a reduced voltage of ∼ ± 800 mV. All RMSD values were calculated for each monomer with respect to the backbone atoms, excluding the flexible TM3–TM4 loop (Figure S4).

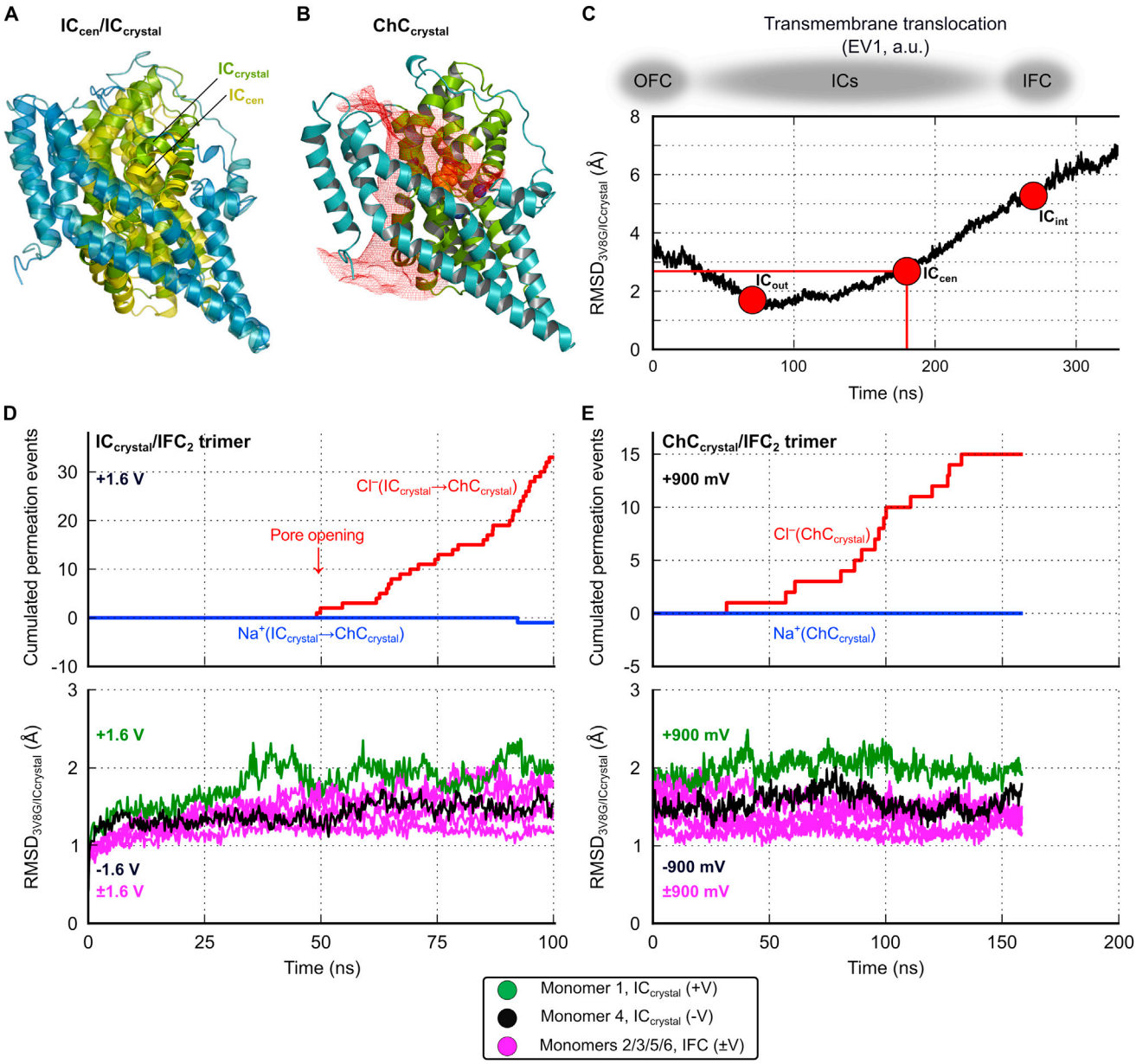

Figure S2. Structural and Functional Comparison of Simulated ICs and a Crystallographic Intermediate, Related to Figure 1

(A) Overlay of the simulated intermediate IC$_{cen}$ and the crystallographic IC$_{crystal}$ (PDB ID code 3V8G) in side view (from within the membrane). Both structures were fitted with respect to their static trimerization domains (blue/cyan) to highlight the different positioning of the IC$_{crystal}$ transport domain (green), which is closer to the OFC conformation domain than is the IC$_{cen}$ transport domain (yellow).

(B) Cl$^-$ distribution around ChC$_{crystal}$ (0.2σ) at +800 mV shows an anion conduction pathway similar to the one seen in simulations of IC$_{cen}$/ChC$_{cen}$ (Figure 1D).

(C) Structural comparison of the OFC–IFC essential dynamics simulation trajectory with the IC$_{crystal}$ structure. Root-mean-square deviation (RMSD) values were calculated between monomer 1 (that underwent OFC–IFC transition in molecular dynamics simulations) and the intermediate IC$_{crystal}$ in the asymmetric crystal structure (PDB ID code 3V8G). The I$_{cen}$ snapshot at 180 ns (mainly used in this study) has an RMSD of 2.7 Å with respect to the crystal structure. The structure closest to IC$_{crystal}$ has a deviation of 1.3 Å, which is below the level of crystallographic resolution (Verdon and Boudker, 2012).

(D) Permeation count and RMSD stability of the IC$_{crystal}$/IFC$_2$ trimer at ~ ± 1.6 V.

(E) Continuation of the simulation with the conducting conformation ChC$_{crystal}$/IFC$_2$ taken from the previous simulation (E) at 100 ns at a reduced voltage of ~ ± 900 mV.

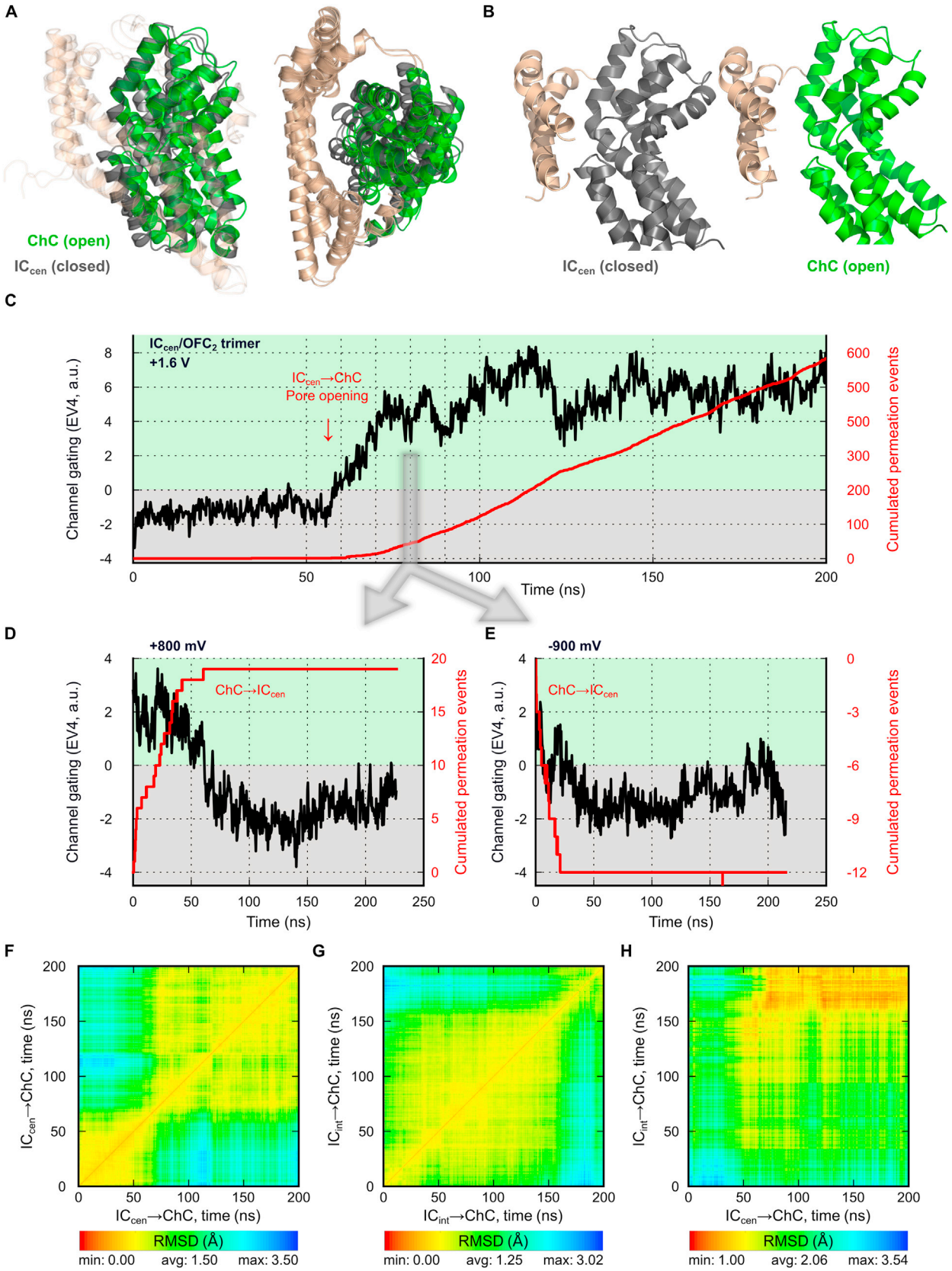

(legend on next page)

Figure S3. Voltage-Dependent and Reversible Channel Gating, Related to Figure 1

(A) Superposition of the monomeric closed intermediate conformation (IC_{cen}) and open channel conformation (ChC_{cen}) (left, side view, from within the membrane; right, top view, from the extracellular space). Structures were fitted onto each other by superimposing the trimerization domains (wheat) to demonstrate that lateral movement of the transport domain results in a broadening of the domain interface and opening of the anion conduction pathway.

(B) Close-up view in perspective from the TM4–TM5 loop (as in Figure 3B) on IC_{cen} and ChC_{cen}. The protein is colored as in (A).

(C–E) The IC_{cen}–ChC_{cen} transition is represented by the fourth eigenvector (EV4) derived from a principal component analysis, and correlates with ion permeation (Figures 1E and S1). The Glt_{Ph} anion channel in the IC_{cen} conformation opens upon depolarization and closes upon hyperpolarization. The data refer to a single, representative simulation of IC_{cen} starting at +1.6 V (C) and using the ChC_{cen} snapshot at 80 ns for continuation at +800/−900 mV (D, E).

(F–H) Root-mean-square deviation (RMSD) matrices of the IC_{cen}–ChC and IC_{int}–ChC gating transitions indicate the convergence of different intermediate closed states to similar open channel conformations. Intra-trajectory RMSD plots quantify the conformational changes starting from IC_{cen} or IC_{int} (F, G). Inter-trajectory RMSD data compare the different conformational changes with one another (H). All RMSD values were calculated for the backbone atoms excluding the flexible TM3–TM4 loop (Figure S4) and are given as color code and minimum, maximum, and average value for each plot.

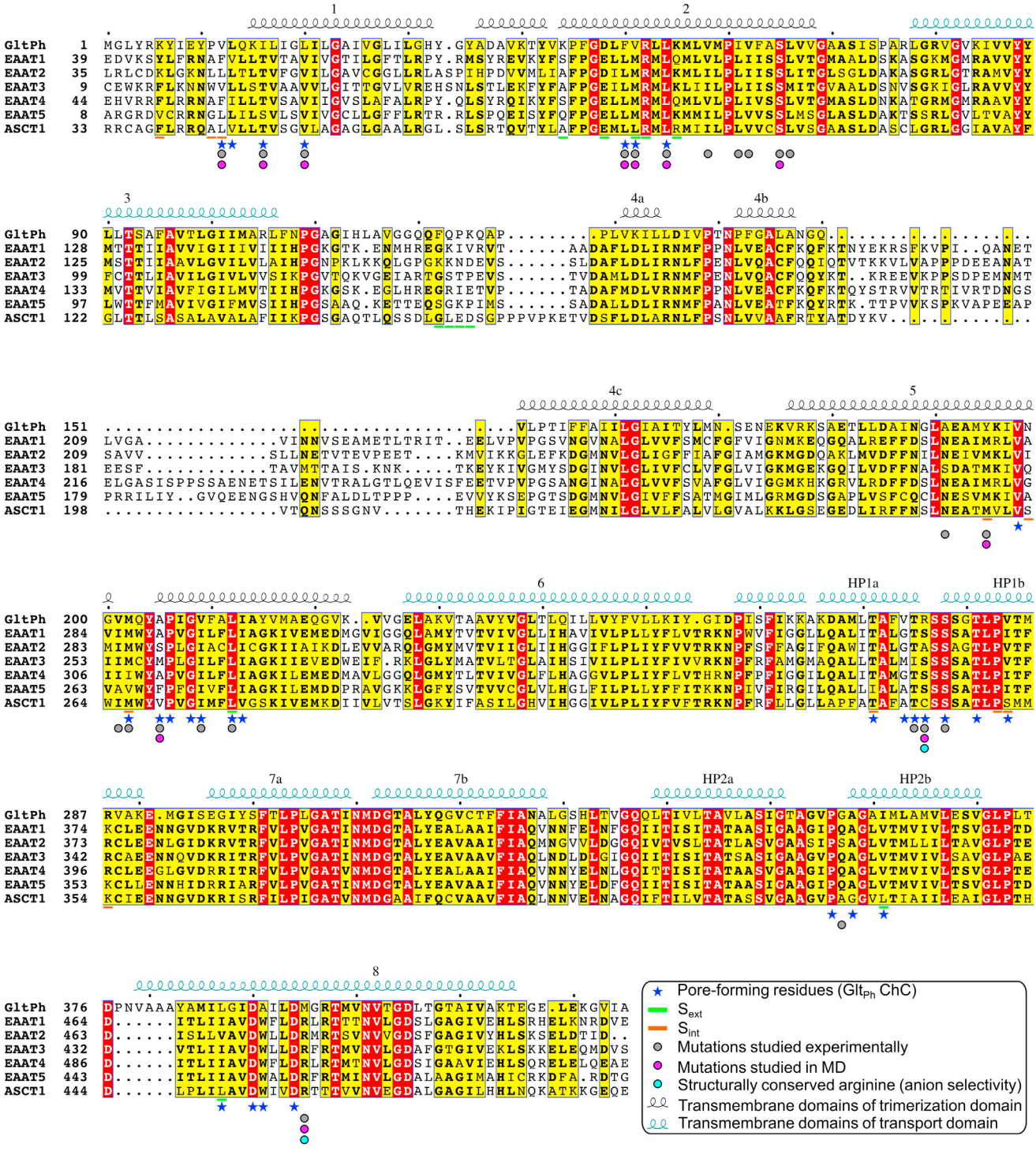

Figure S4. Sequence Alignment of Glutamate Transporter Family Proteins, Related to Figure 3

Alignment of amino acid sequences of Glt_{Ph}, human EAATs 1–3 and EAAT5, rat EAAT4 and human ASCT1. Stars mark residues close to permeating anions in molecular dynamics (MD) simulation and circles denote residues that have been exchanged experimentally and/or in simulations.

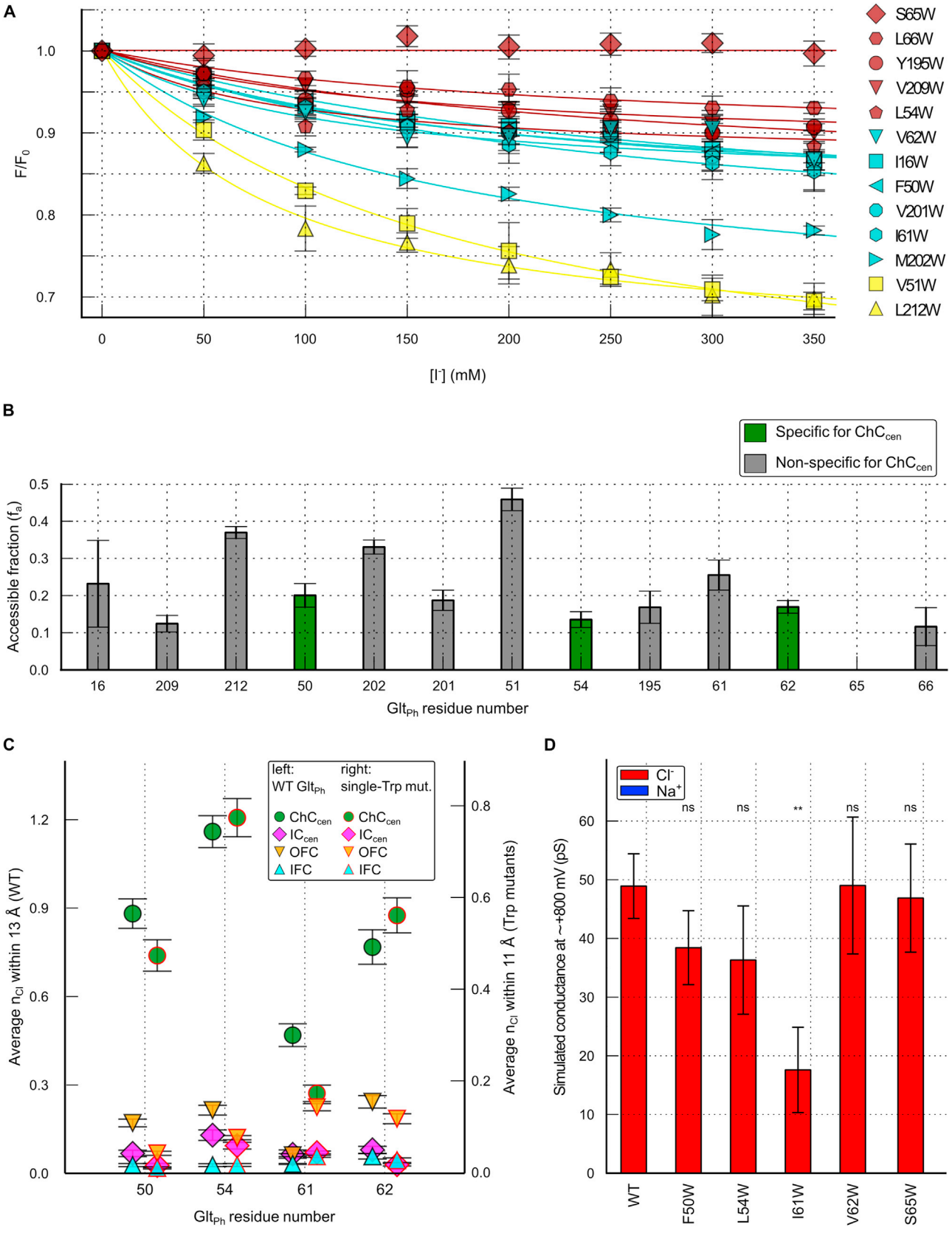

(legend on next page)

Figure S5. Iodide-Accessible Fraction f_a of Various Glt_{Ph} Single-Tryptophan Mutants, Related to Figure 4

(A) $[I^-]$ dependence of relative fluorescence levels for WT and mutant Glt_{Ph} (means ± SE; n ≥ 5 for each). The data are identical to those shown in Figure 4C. Solid lines are fits with the inverted modified Stern–Volmer equation $F/F_0 = f_a/(1+K_{SV}\cdot[I^-])+1-f_a$ to experimental data using least-squares. The f_a values depend on the location of the tryptophan, as well as on shifts in the conformational equilibrium of the transporter induced by the mutations. In the case of tryptophan residues predicted to be exclusively accessible in the ChC open channel conformation (Figure 4D), f_a values of > 0 provide experimental evidence for the formation of the anion-conducting pore in vitro. The f_a value could not be determined for S65W because this mutation did not exhibit an iodide-induced reduction in fluorescence intensity. This parameter has a physical meaning only if there is a single quencher-accessible conformation (see residues 50, 54, and 62).

(B) Summary of f_a values (means ± SE; n ≥ 5 for each) obtained by fitting inverted modified Stern-Volmer equations to the results from (A) (see the Extended Experimental Procedures).

(C) Comparison of predicted anion accessibilities of WT side chains (data from Figure 4D) or around tryptophan side chains using simulations of the respective single-tryptophan mutant for various conformations (left symbols/black edge, analysis of WT Glt_{Ph}; right symbols/red edge, analysis of single-tryptophan mutants). Data shown are average numbers of Cl^- ions (±SD) within a distance threshold of 13 or 11 Å to the side chain center-of-mass of the WT or the tryptophan side chains, respectively.

(D) Cl^- conductances (±SD) at +800 mV derived from simulations of F50W, L54W, I61W, V62W and S65W Glt_{Ph} demonstrate that all of these mutants can conduct anions, although some mutations affect the conductance.

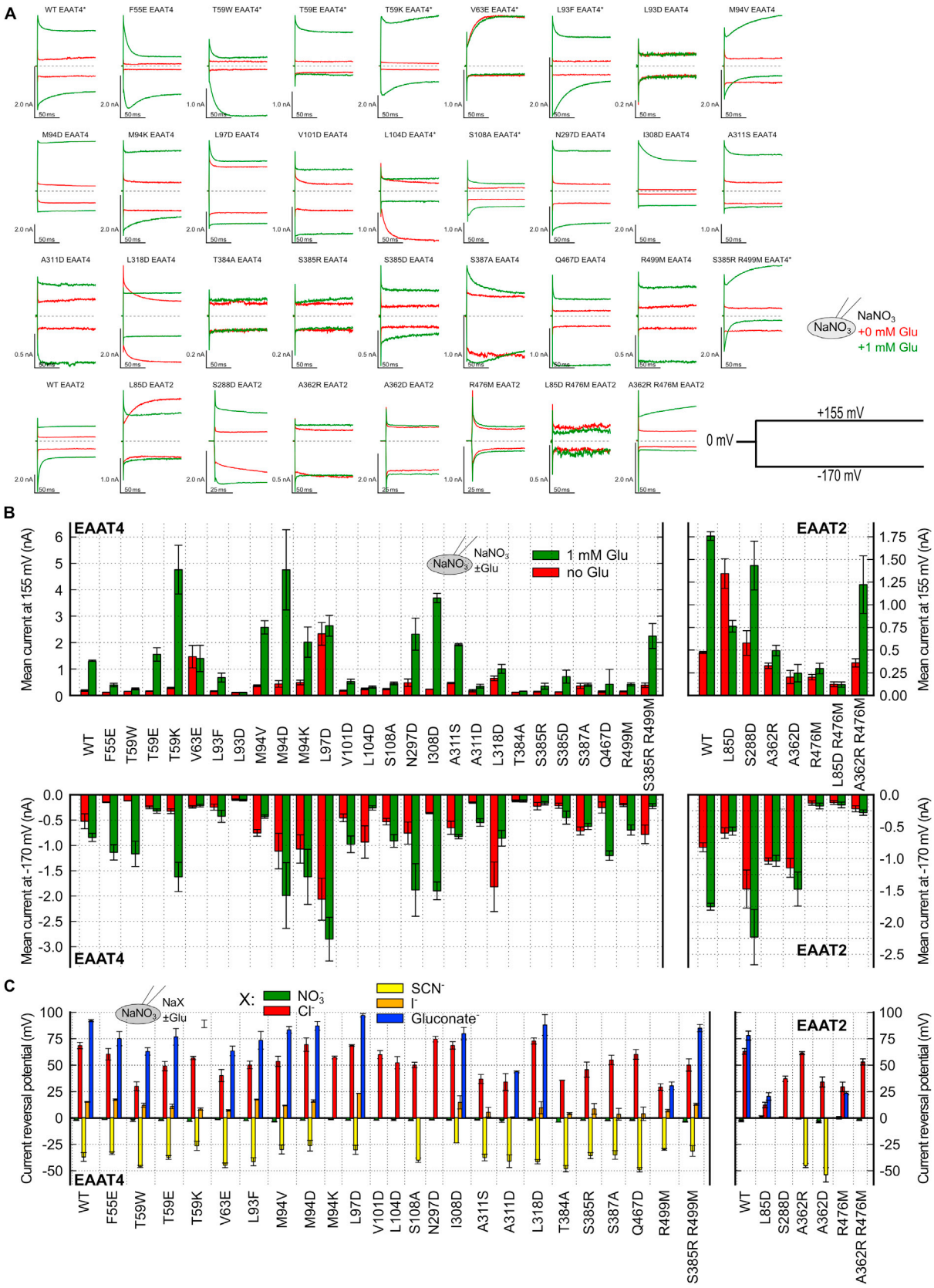

(legend on next page)

Figure S6. Electrophysiological Analysis of EAAT2/4 Mutants, Related to Figures 6 and 7

(A) Representative whole-cell current traces in the presence and absence of extracellular glutamate of wild-type (WT) EAAT2/4 and all mutants used in this study. Asterisks indicate constructs used for noise analysis.

(B) Mean whole-cell steady-state anion current amplitudes in the absence and presence of glutamate at positive and negative potentials (means ± SE; n=6–13). Note that whole-cell conductances do not necessarily correlate with single-channel properties (as determined by noise analysis in Figure 6) because these mutations affect both anion permeation and channel gating, i.e., the channel open probability.

(C) Mean current reversal potentials using 115 mM NO_3^- as the main intracellular anion and various extracellular permeant and impermeant (gluconate) anions (means ± SE; n=6–13).

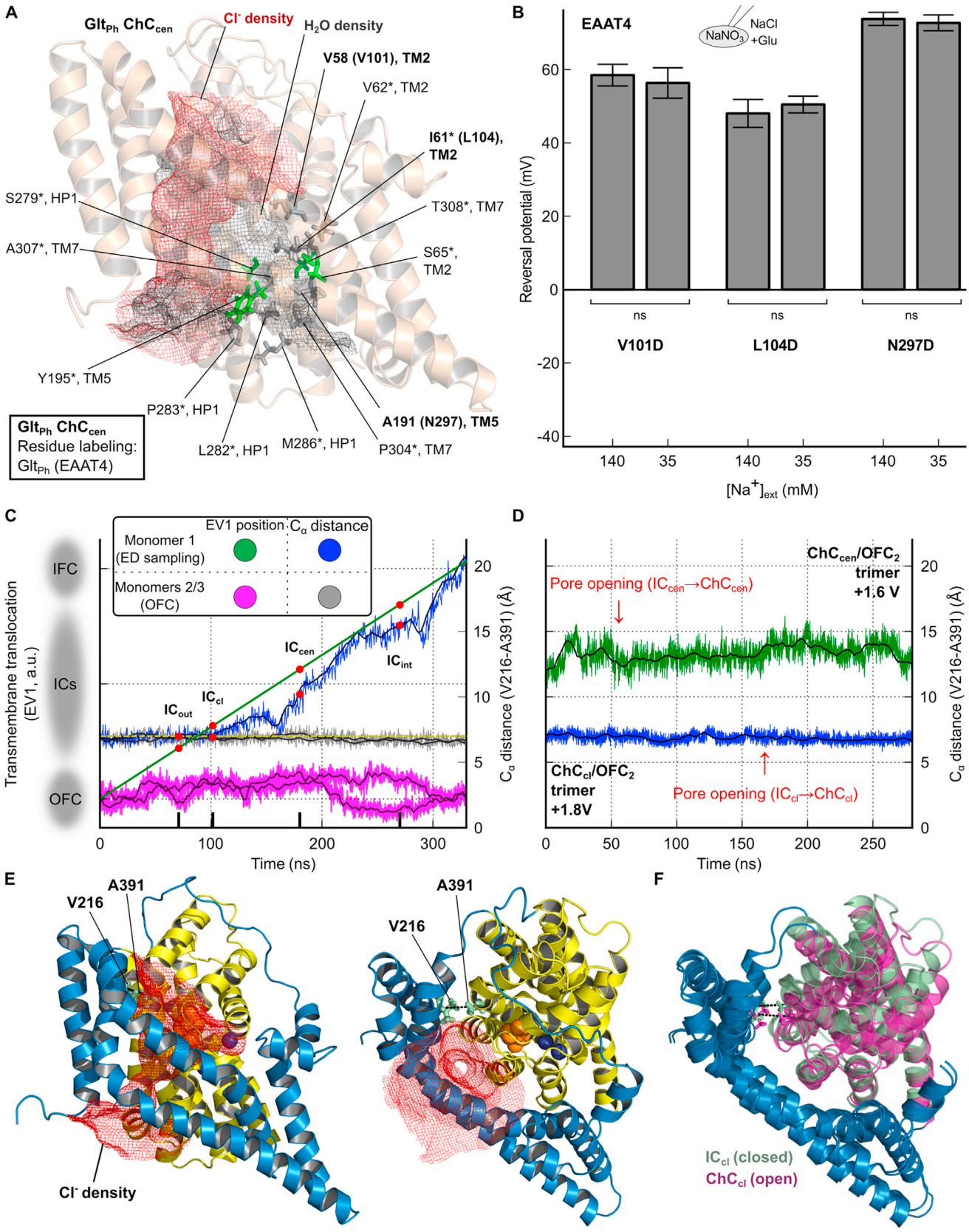

(legend on next page)

Figure S7. Mutations along a Proposed Alternative Pathway and Interdomain Crosslinkage Do Not Disrupt Glt_{Ph}/EAAT Anion Conduction, Related to Figures 6 and 7

(A) Stick representation of side chains in the ChC_{cen} Glt_{Ph} structure (side view) lining a protein cavity around S65, as observed in the crystallized intermediate structure (PDB ID code 3V8G). Asterisks indicate residues lining this "S65 path," which has been speculated to be responsible for anion conduction (Ryan et al., 2004; Verdon and Boudker, 2012; Cater et al., 2014). For comparison, the Cl^- density along the anion channel identified in this study is shown as red mesh (Figure 1D). The black mesh illustrates the water density observed in the trimerization/transport domain interface of ChC_{cen}. Side chains are colored according to Figure 3A (red, negative; green, polar; gray, apolar).

(B) Current reversal potentials for mutant EAAT4 carrying aspartate substitutions of the homologous residues of V58, I61 and A191 of Glt_{Ph}, which line the "S65 path" (compare the experiments with Figure 7B). The identity of reversal potentials at different external [Na^+] demonstrates the absence of cation permeability for V101D, L104D and N297D EAAT4 in patch-clamp recordings (means ± SE; n = 4–5 for each).

(C) Time course of essential dynamics (ED) sampling simulation of transmembrane translocation performed on a single monomer (the other two monomers were unaffected in the OFC), replicated from Figure S1C. Black lines represent running averages. In addition, the evolution of the distance between the C_α atoms of V216 and A391 during OFC–IFC transition is shown. The maximum C_α distance of ~7 Å between cross-linked cysteines found in proteins (Katz and Kossiakoff, 1986), is illustrated by the yellow dashed line. Red circles indicate both y axis positions of IC_{int}, IC_{cen} and IC_{out} and IC_{cl}, the latter of which was selected as an intermediate with the most central location and a C_α distance of $\leq$ 7 Å for modeling cross-linkage between these two residues (B–D).

(D) Molecular dynamics simulation of pore opening and Cl^- permeation in the presence of the indicated transmembrane voltage of cross-linked V216C–A391C Glt_{Ph}. The conformation used is IC_{cl} (A) and the cross-link is modeled on the WT protein by a restraint to maintain a C_α distance of $\leq$ 7 Å between V216 and A391. For comparison, time-dependent changes in the C_α distance between V216 and A391 of WT Glt_{Ph}, i.e., of IC_{cen} without distance restraints, are shown (Figure 1). WT dynamics show an increasing distance between these two residues preceding pore formation.

(E) Cross-linkage does not prevent anion permeation along the identified anion conduction pathway (left, side view of a ChC_{cl} monomer; right, top view; Figure 1D), consistent with recent experimental findings for the homologous cysteine mutant of EAAT3 (Shabaneh et al., 2014). Residues V216 and A391 are shown in stick representation and the black dotted lines indicate a C_α distance restraint of $\leq$ 7 Å.

(F) Overlay (top view) of the closed IC_{cl} and the corresponding open channel conformation ChC_{cl} of cross-linked Glt_{Ph}. The V216–A391 distance restraint represents an inter-domain cross-link that partially tethers the transport and the trimerization domains. This cross-link reduces overall protein flexibility, but does not abolish anion pore formation (compare Figure 1C).

See also Table S1.